

16
12

AD-A266 060



Final Research Report:

"Quantum Dynamics of Helium Clusters"

Grant no.: N00014-89-J-1755

March 1989 - March 1993

DTIC
ELECTE
JUN 17 1993
S A D

Principal Investigator

K. B. Whaley
Department of Chemistry
University of California
Berkeley, CA 94720

This document has been approved
for public release and sale; its
distribution is unlimited.

This document is approved for public release

93 6 10 009

323
11

93-13580



44pt

**Best
Available
Copy**

Introduction

Our study of helium clusters was motivated by the desire to understand the scaling of the unusual properties of bulk ${}^4\text{He}$, a quantum liquid, in finite size systems as one goes from the macroscopic regime to the regime of molecular dimensions. This is fully in the spirit of general cluster research, namely to develop our understanding of how the transition from molecular to bulk systems (or vice versa) is reflected in the internal structure and dynamics of finite size aggregates. The unique feature of helium is its dominant quantum behavior, resulting from a low mass and weak interatomic binding energy. Clusters of helium are therefore very weakly bound van der Waals species, whose properties were expected to be dominated by zero point delocalization effects. During this grant period, we devoted our attention exclusively to clusters of ${}^4\text{He}$, which are bose systems. These are more strongly bound than the fermionic species ${}^3\text{He}_N$, and are also easier and cheaper to study experimentally. Furthermore, analogy with the bulk behavior suggests that any superfluid effects if present will occur at considerably higher and therefore experimentally more readily accessible temperatures for the ${}^4\text{He}$ species. In addition to the helium clusters, we also applied our Monte Carlo techniques to clusters of molecular hydrogen, which for $J=0$ are also Bose clusters. These are more strongly bound than clusters of helium, yet are still very delocalized by chemical standards and offer an intriguing possibility of a new superfluid.

Goals of original research plan

- 1) To understand the size-dependent scaling of superfluid behavior or analogous collective effects in clusters of ${}^4\text{He}_N$. As a preliminary step this involved analysis of Bose-Einstein condensation in a weakly interacting bose cluster.
- 2) Despite much phenomenological progress in the understanding of superfluidity in bulk helium II, a molecular description for the characteristic excitations of bulk helium found only in the superfluid state was still missing. By developing a truly microscopic theory of collective excitations in these quantum clusters involving accurate ground and excited state wavefunction information, we aimed to achieve new insight into the atomic dynamics underlying the superfluid state in bulk He II by identifying and analyzing the behavior in finite sized clusters .
- 3) Determination of feasible experimental probes of the cluster dynamics, in particular of charged species or of non-dissociative molecular probes. This goal is further related to the more long term aim of employing the unusual physical properties of these quantum clusters to modify and control the course of chemical reactions of embedded/attached species at ultra-low temperatures.
- 4) Development of Monte Carlo methods to provide accurate ground and excited state wavefunctions for the ${}^4\text{He}_N$ clusters. This original aim was extended to deal also with the more strongly bound (H_2) $_N$ species, which have more solid-like character.

Goals achieved during grant period

Our central achievements attained during the grant period are the following:

- 1) Establishment of a new quantum liquid drop theory for the collective excitations of these Bose clusters, (papers 1, 2, 4). Together with the accurate ground state wavefunctions described below, this led to calculations of the compressional excitation spectrum for $L = 0$ (spherically symmetric) and $L = 1$ (dipole) symmetry, for a range of cluster sizes. The size scaling of the excitation spectrum showed the onset of a roton minimum at sizes $N \sim 100$, leading to the important physical conclusion that cluster of size $N \geq 100$, corresponding to diameters $R \geq 10 \text{ \AA}$ can support superfluid flow.
- 2) Development of accurate Monte Carlo methods for ground state wavefunctions of general quantum clusters (papers 5, 7, 8, 11). These consisted of both variational and (exact) diffusion Monte Carlo techniques. While the basic 'unguided' Metropolis sampling of variational cluster wavefunctions had been previously employed by the nuclear physics community, we improved the accuracy and sampling techniques considerably, by developing new variational wavefunction forms and using guiding functions to optimize sampling at small interparticle separations. This resulted in an unprecedented precision of $\sim 5\%$ in density profiles in the interior of the cluster, and led to an unexpected discovery of a large collinear contribution to the structure of the He_3 trimer (paper 7). Application of diffusion Monte Carlo to these weakly bound atomic systems is new, and was performed selectively to calibrate the variational results (paper 8). The diffusion Monte Carlo algorithm was modified to employ a constant ensemble size (paper 11), and also to allow modifications of the quantum force in regions of small inter-particle distance (paper 8). High accuracy for relatively large cluster sizes was achieved as a result of refining the original diffusion Monte Carlo algorithm (papers 8, 11). These exact calculations show structure in both density profiles and pair distribution functions which is compatible with some very weak hard-core packing effects. No such structure is observed at the variational level.
- 3) Development of a quantum theory for atomic and molecular impurities in helium clusters (papers 7, 11). This has so far been restricted to ground state impurities, and consists of a variational approach to the new cluster containing the impurity, in which the latter interacts pairwise with the helium atoms. The variational wavefunction is extended to include pairwise correlation terms between the impurity and the helium.

This approach was applied first to a H_2 impurity attached to He_N , $N = 2 - 19$, and structural analysis of the resulting mixed cluster ground state made (paper 7). The lighter impurity H_2 is extensively delocalized throughout the cluster, with a peak in the vicinity of the diffuse surface region. Quantitative analysis showed that the H_2 is however still largely in the interior of the cluster for this range of sizes. The He_{13} species is unique in the extent to which it expels the H_2 , suggesting an unusual structural stability which may be associated with an icosahedral unit. This is particularly significant in light of the absence of any energetic magic numbers for neutral helium clusters. Subsequent unpublished calculations for a D_2 impurity show quite a different situation, with the

heavier D_2 species considerably more localized at the cluster center, and with no peak in or near the surface region. The helium distribution is complementary to the D_2 distribution, showing a peak away from the cluster center. However for the trimer species D_2He_2 the central peak corresponding to near collinear configurations still persists.

Both variational and diffusion Monte Carlo approaches were then applied to the analysis of SF_6 in He_N (paper 11). This is a much more complex system, due to both a greater binding of the impurity with He, and also to the marked anisotropy of the He- SF_6 interaction potential. New trial wavefunctions were developed which faithfully incorporated the main features of the potential anisotropy. Calculations were made for clusters SF_6 with N varying from 1 (the 'dimer') to $N=499$. The ground state structures of these systems showed pronounced localization of the helium around a centrally located SF_6 impurity. This localization occurs in sequential shells, with the first, nearest neighbor shell containing about 22-23 atoms at a density comparable to that of bulk solid He at ~ 100 atmospheres. The shells further away from the impurity contain successively larger numbers of He atoms, and for sizes up to $N=499$ are still at densities lower than that of bulk liquid helium. However it is interesting that the exchange energy for substitution of one He by the impurity (paper 7) appears nevertheless to have saturated by $N=111$, despite the fact that the structure has not converged to what we expect for an SF_6 impurity in bulk helium. For SF_6 we also analyzed the spectral shifts of the ν_3 vibrational absorption lines due to the instantaneous dipole-induced dipole (IDID) interactions with the surrounding 'solvent' helium species. This was motivated by recent experimental measurements of such shifts for SF_6 in He_N (Goyal, S., Schutt, D. L., and Scoles G., Phys. Rev. Lett. **69**, 933 (1992)) and in $(H_2)_N$, (Goyal, S., Schutt, D. L., Scoles G., and Robinson, G. N., Chem. Phys. Lett. **196**, 123 (1992)). We find a red-shifted absorption, which increases with size to a value of ~ 0.93 cm^{-1} for $N=111$, with a half-width of ~ 0.25 cm^{-1} . This is somewhat smaller than the experimental value (~ 1.5 cm^{-1}) which also differs from our calculation by being split into two components. The most likely reason for this difference is that in the experiment the clusters are not in the ground state, but gain a considerable amount of angular momentum from pick-up of the impurity. Large amounts of angular momentum cause considerable centrifugal distortions, as we summarize in 4) below, and may cause the SF_6 to be located in an asymmetric position which can give rise to a line splitting, e.g., at a cluster surface. This possibility can be investigated with Monte Carlo techniques based on trial wavefunctions combining the features of these impurity functions, and of the excited rotational states described below. Such studies are planned for future work.

- 4) Development of quantum theoretical approaches to excited states for the collective modes (papers 2, 5, 10). This began with a variational approach to excited compressional states which was based on the Feynman operator approach (papers 2, 5). The first four excited compressional states for $L = 0$ were calculated variationally for $N = 240$, maintaining orthogonality to lower states by a generalized Gramm-Schmidt procedure. These results showed a significant lowering of the compressional energies relative to both classical estimates based on the conventional macroscopic liquid drop model, and also to our new quantum liquid drop model. We have recently extended the variational approach to excited states of overall rotation of the cluster, employing a different approach from the Feynman

excitation operator (paper 10). New trial functions which are eigenfunctions of total angular momentum and which are physically motivated to have rotational rather than vibrational character, were developed, and employed in both variational and fixed node diffusion Monte Carlo studies of He_7 and of its more strongly bound counterpart $(\text{H}_2)_7$. The rotational energies are considerably lower than the compressional energies studied previously (papers 2, 5). The rotationally excited states for He_7 were found to be metastable with respect to dissociation for $L \geq 2$, while $(\text{H}_2)_7$ is metastable only for $L \geq 6$. Both species showed very large oblate centrifugal distortion at low L values, which developed to diffuse toroidal distributions at large L . The distribution of the cluster surface clearly changes, which has possible consequences on the distribution and spectral shifts of impurities such as SF_6 (see 3) above).

5) The ground and excited state Monte Carlo techniques developed for helium clusters have also been applied to clusters of H_2 ($J = 0$), which is also a Bose system (papers 6, 10, 12). We introduced an additional element of employing 'shadow wavefunctions' for fictitious particles representing lattice sites here in order to allow for more rigid structures. The primary goal of this extension of our helium studies is to determine whether a liquid-like ground state exists for $(\text{H}_2)_N$ for N small, and if so, whether these clusters display similar superfluid behavior to He_N . Our preliminary results (paper 6) showed that the smallest clusters ($N \leq 7$) are extensively delocalized. More recent results based on a more accurate trial wavefunction and on subsequent diffusion Monte Carlo calculations (paper 12) show that clusters up to $N = 33$ still show strong delocalization, although weak features characteristic of solid like close packed structures are now also apparent. We have analysed the structure of both these and the He_N clusters in the body fixed frame by computing principal moments of inertia, thereby avoiding the orientational averaging implicit in usual Monte Carlo sampling for finite systems.

Publications resulting from grant

1. M.V. Rama Krishna and K. B. Whaley, "Collective Excitations of Helium Clusters," *Phys. Rev. Lett.* **54**, 1126 (1990).
2. M.V. Rama Krishna and K.B. Whaley, "Microscopic Studies of Collective Spectra of Quantum Liquid Clusters" *J. Chem. Phys.* **93**, 746 (1990).
3. M.V. Rama Krishna and K. B. Whaley, "Superfluidity in Helium Clusters" in "*On Clusters and Clustering: from Atoms to Fractals*", ed. P. J. Reynolds, (Elsevier, Amsterdam, 1993).
4. M.V. Rama Krishna and K.B. Whaley, "Structure and Excitations of Quantum Liquid Clusters" invited article, *Modern Physics Letters B* **14**, 895 (1990).
5. M.V. Rama Krishna and K.B. Whaley, "Wavefunctions of Helium Clusters", *J. Chem. Phys.* **93**, 6738 (1990).
6. M.V. Rama Krishna and K. B. Whaley, "The Structure of Small Molecular Hydrogen Clusters", *Z. Phys. D.*, **20**, 223 (1991).
7. R.N. Barnett and K.B. Whaley, "Monte Carlo Study of Impurities in Quantum

Clusters: $H_2^4He_N$, N=2-19" J. Chem Phys., **96**, 2953, (1992).

- 8. R.N. Barnett and K.B. Whaley, "Variational and Diffusion Monte Carlo for Quantum Clusters", Phys. Rev. A., **47**, 4082, (1993).
- 9. K. B. Whaley, "Structure and Dynamics of Quantum Clusters" (invited review for Internation Journal of Physical Chemistry, in press 1993).
- 10. M. McMahon, R. N. Barnett and K. B. Whaley, " Rotational Excitations of Quantum Liquid Clusters", (J. Chem. Phys., submitted May 1993).
- 11. R. N. Barnett and K. B. Whaley, "Molecules in Helium Clusters: SF_6He_N ", (J. Chem. Phys., in preparation).
- 12. M. McMahon and K. B. Whaley, "Monte Carlo Studies of Molecular Hydrogen Clusters: $(H_2)_N$, N=7, 13, and 33" (Chem. Phys. Lett., in preparation).

Superfluidity in Helium Clusters

M.V. Rama Krishna*† and K.B. Whaley*

20.1 Introduction

Theoretical and experimental investigations of clusters has been an active and growing area of research for the past several years. Yet, much of our current understanding of the structure, dynamics, and energetics of clusters is based on essentially "classical" clusters. By this we mean that although quantum mechanics is important in the description of their electronic structure, it does not play a role in the statistical behavior of the atoms (or rather, of the nuclei) themselves. However, when the atoms in the cluster are light, such as H or He, quantum mechanics plays a significantly different role. It is thus important to study quantum clusters in order to understand what role quantum statistical effects may play in clusters, and how the uniquely quantum phenomena such as superconductivity and superfluidity are modified in finite systems. With this in mind we will discuss clusters of ${}^4\text{He}$, which obey Bose statistics. The goals are threefold: 1) to understand how superfluidity manifests itself in helium clusters, 2) to determine the energy level spectra of these clusters, and 3) to establish experimental probes of these clusters.

20.2 Transition Temperatures

Bulk liquid ${}^4\text{He}$ is known to undergo a phase transition from a normal to a superfluid state at about 2.17 K. This phase transition is characterized by a nearly logarithmic divergence of the heat capacity, and by the fact that the superfluid phase can flow through fine capillaries with zero viscosity.^[1] Quantum statistics is the key to this effect. For example, liquid ${}^3\text{He}$, which is made of fermions, exhibits superfluid behavior only at a much lower temperature of about 1×10^{-3} K. This difference is not simply a mass effect, but results from the need of the ${}^3\text{He}$ nuclei to pair to form effective Bose particles. Other symmetry related properties are significant as well. For example, if one models liquid ${}^4\text{He}$ as a non-interacting Bose gas one finds that this model exhibits a cusp in the heat capacity curve at about the same temperature where the experimental heat capacity curve exhibits divergency.^[2]

Given these observations, and their relation to the quantum behavior of the particles making up liquid ${}^4\text{He}$, we wish to understand how the phase transition is modified in ${}^4\text{He}_N$ clusters due to finite-size effects. Although there is no longer a true phase transition in clusters, it is reasonable to use the same ideas that have been previously used to understand the phase tran-

* Department of Chemistry, University of California, Berkeley, CA 94720.

† Present address: Box 955 Havemeyer Hall, Columbia University, New York, NY 10027-6948.

sition in bulk liquid ^4He . Consequently, we begin by discussing the "transition temperatures" and the condensate fractions for clusters.

The Bose-Einstein (BE) condensation temperature of a non-interacting Bose gas of density ρ is given by^[3]

$$\begin{aligned} T_{BE} &= \frac{2\pi\hbar^2}{mk_B} \left(\frac{\rho}{2.612} \right)^{2/3} \\ &= 4.015 \times 10^{-15} \rho^{2/3} \text{ K.} \end{aligned} \quad (20.1)$$

For liquid helium, Eq. (20.1) gives $T_{BE} = 3.13$ K, which is 0.96 K larger than the experimental value.^[1, 2] We used Eq. (20.1) to calculate T_{BE} of helium clusters, with the modification that we subtract 0.96 K from the computed values so that for sufficiently large clusters we recover the experimental bulk value of T_λ correctly. These corrected \tilde{T}_{BE} are given in Table 20.1. The densities of the clusters are determined using $\rho = 3/(4\pi r_0^3)$, where the r_0 are the calculated unit radii.^[4]

One can use Ginzburg-Landau-Pitaevskii (GLP) theory to estimate the transition temperatures of the interacting system.^[5] This is a phenomenological theory in which the free energy density is expanded in terms of the order parameter, which here is an effective complex wavefunction of the fluid. The expansion is valid only when the order parameter is small and the coherence length, which is the length scale over which the order parameter changes, is large. Consequently, this theory is applicable only when the temperature T of the fluid is close to T_λ . In the original mean-field GLP theory, the expansion coefficients were functions of integer powers of $(T_\lambda - T)$.^[5] Such a mean-field approach neglects fluctuations, which are very important close to T_λ . The modern version of this theory due to Mamaladze employs a modified free energy density that accounts for the fluctuations of the order parameter near T_λ by taking the temperature dependence of the expansion coefficients from experiments.^[6, 7] The successful applications of this modified GLP theory to the prediction of transition temperatures of helium films and pores^[7, 8] gives us confidence regarding its utility in the case of clusters. Clearly this theory can not predict critical exponents as these are put in *via* the expansion coefficients. However, these exponents can also be obtained from first principles starting from the GLP theory and using the renormalization group theory of Wilson. For our purposes here this is not necessary.

When applied to a spherical cluster, the modified GLP theory predicts the transition temperature T_λ to be given by^[7]

$$T_\lambda = T_\lambda^b - \frac{25.3}{R^{\frac{3}{2}}} \text{ K.} \quad (20.2)$$

where R is the radius of the cluster in Å, T_λ^b is the transition temperature of bulk liquid helium, and T_λ is that of the cluster. Of course, although the transition temperature is a sharply defined quantity in macroscopic systems, in clusters we expect that there is rather a temperature range over which the transition to the superfluid state takes place. The temperatures predicted above essentially give the location of the peak values of the rounded heat capacity curves of the clusters.

To calculate the condensate fraction in these clusters at $T = 0$ K, let us use the model of

Table 20.1: Transition temperatures and zero-temperature condensate fraction in helium clusters. (R is given in Å, \bar{T}_{BE} and T_λ in Kelvin.)

N	R	\bar{T}_{BE}	T_λ	%C
20	7.4	1.1	0.9	32.7
40	8.8	1.4	1.2	27.1
70	10.2	1.6	1.4	22.6
112	11.8	1.6	1.5	21.2
240	14.7	1.8	1.7	17.1
728	20.9	1.9	1.9	15.0
10000	47.8	2.1	2.1	12.2
Liq. He	∞	2.17	2.17	9.2

an imperfect Bose gas for the clusters. This is given by^[9]

$$\frac{N_0}{N} = 1 - \frac{8}{3\sqrt{\pi}} a^{3/2} \rho^{1/2} \quad (20.3)$$

$$= 1 - 6.148 \rho^{1/2}, \quad (20.4)$$

where $a = 2.556$ Å is the experimental scattering length of the helium atoms. The percent condensation %C is simply $N_0/N \times 100$. These results are given in Table 20.1.

We see from Table 20.1 that the theoretical estimates of \bar{T}_{BE} and T_λ agree remarkably well even for a cluster as small as twenty atoms, and that the bulk transition temperature is depressed by only about 0.5 K in He_{240} . We also find that the condensate fraction approaches that of the bulk fluid rather rapidly. Note that the condensate fraction is decreasing as T_λ is increasing. This indicates that the strong interactions between particles in the denser (larger) clusters are depleting the zero temperature condensate, while increasing the transition temperatures.

20.3 Collective Excitations

Another quantity related to superfluidity is the excitation spectrum.^[2] For a microscopic understanding of superfluidity, it is important to understand how the collective excitation spectra of clusters change as a function of cluster size, and how they approach that of the bulk fluid. With this goal in mind, consider helium clusters as quantum liquid drops of radius R and uniform interior density ρ_0 . The density wave excitations of the droplet are characterized by the quantum numbers (l, m) and n . The momenta k_{ln} of these excitations are given by the boundary condition $j_l(k_{ln} R) = 0$. Within this liquid drop model a harmonic analysis of the collective vibrations of the cluster gives^[10, 11]

$$\epsilon_{ln} = \frac{\hbar^2 k_{ln}^2}{2mS_l(k_{ln})\nu_{ln}}. \quad (20.5)$$

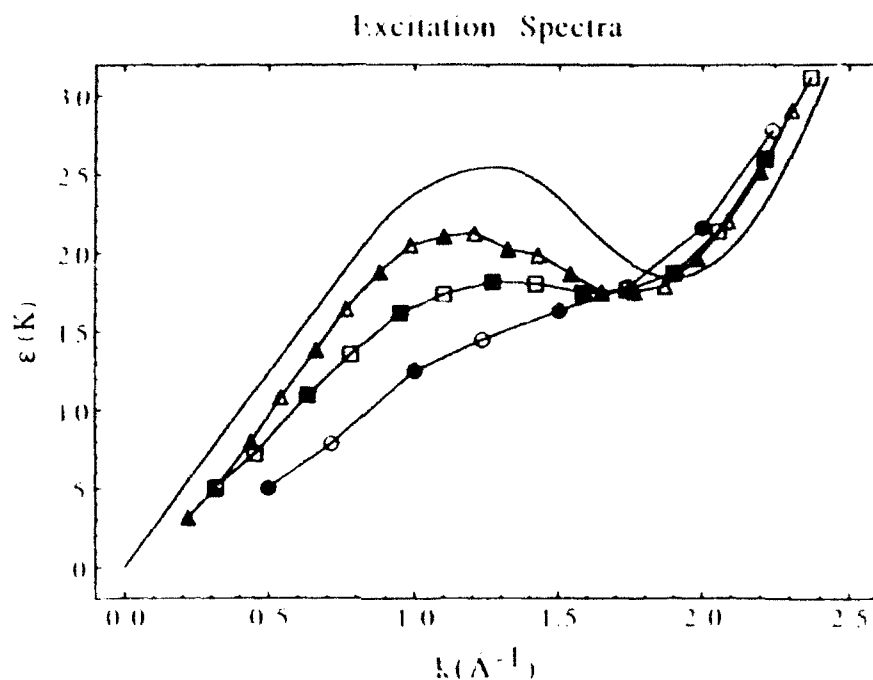


Figure 20.1: Excitation spectra of $l = 0$ and 1 modes obtained using Eq. (20.5) for $N = 20$ (circle), 70 (square), and 240 (triangle) clusters. The filled symbols give $l = 0$ spectra and the open ones give $l = 1$ spectra. The solid line (—) is the Bijl-Feynman excitation spectrum of bulk He II.

where S_l is the structure function of the cluster, defined as the Fourier Bessel transform of the density-fluctuation-density-fluctuation correlation function, and ν_{ln} is the normalization factor for the spherical Bessel functions. Complete details of the theory and calculations are given in Refs. 10, 11.

Equation (20.5) is the finite cluster analog of the Bijl-Feynman excitation spectrum for bulk liquid helium.^[11] It represents the compressional vibrational excitation energies of the cluster, and in the bulk limit corresponds to the phonon spectrum of liquid He. To get a picture of these spectra one needs to compute the structure functions S_l . Monte Carlo random walk simulations for $l = 0$ and 1 , and $N = 20$, 70 , and 240 were performed. The spectra, together with the Bijl-Feynman excitation spectrum of liquid helium, are shown in Fig. 20.1. We see that the spectrum of the clusters evolves toward that of the bulk fluid rather rapidly. The pronounced dip at $k \approx 2 \text{ \AA}^{-1}$ in the liquid helium spectrum is known as the roton region. The He_{70} cluster already shows such a roton structure at about 2 \AA^{-1} and the spectrum of He_{240} strongly resembles that of liquid helium. The validity of these results are confirmed by a more general theory based on Bijl-Feynman wavefunctions for the excited states of the clusters.^[11]

Since the excited states of a many-body system play an important role in both the thermodynamics and dynamics of the system, the strong resemblance of the excitation spectra of

He_N clusters to the bulk fluid is indicative that these clusters will also exhibit similar thermodynamic and dynamic behavior. It is reasonable therefore to expect helium clusters of about 100 atoms to undergo a normal \leftrightarrow superfluid transition strongly resembling that of liquid helium. There are additional arguments for making this connection between the excitation spectrum and superfluidity. For example, Bogoliubov first showed that the phonon-roton spectrum of liquid helium is a result of both interactions between Bose particles and the presence of the Bose-Einstein condensate.^[12] (See also Table 20.1 and the associated remarks made in Sec. 20.2.) For the simple model of a weakly interacting Bose gas he obtained

$$\epsilon(k) = \sqrt{\left(\frac{\hbar^2 k^2}{2m} + \frac{U N}{V}\right)^2 - \left(\frac{U N}{V}\right)^2}. \quad (20.6)$$

where $U = 4\pi a/m$ is the interaction energy assumed to be constant and repulsive, and k is the linear momentum associated with the excitation. This yields a linear part (phonon branch) at small momenta and a quadratic piece (free-particle branch) at higher momenta, and thus reproduces the main features of the phonon-roton spectrum of liquid helium. Furthermore, if either U or $\rho = N/V$ is very small, then the spectrum will be completely free-particle like. Such a system will not exhibit superfluidity since the minimum velocity needed to excite the fluid, known as the Landau critical velocity, vanishes in this case.^[2] Other liquids, such as water, which exhibit collective excitations^[13] at large k values ($k \geq 1 \text{ \AA}^{-1}$) also may not exhibit superfluidity because these liquids are stable only at high temperatures. In this regime the thermal excitations dissipate the energy of the moving particles. Although the model of a weakly interacting Bose gas is not quantitatively appropriate for liquid helium, the essential relationship between Bose-Einstein condensation and the phonon-roton spectrum is still present. Hence, the onset of a phonon-roton type spectrum for a Bose fluid is a signature of a large Bose-Einstein condensate and of superfluidity. Based on this argument the results presented in Fig. 20.1 give evidence that clusters of about 70 atoms should be superfluid at sufficiently low temperatures.

Recently, path-integral Monte Carlo simulations have been used to compute heat capacities and superfluid densities of He_{64} and He_{128} clusters as a function of temperature.^[14] The peaks of the computed heat capacity curves yield “transition temperatures” of 1.6 and 1.8 K, respectively, in very good agreement with those reported in Table 20.1 for similar sized clusters. The path-integral simulations also indicate that the width of the heat capacity maximum is increasing while T_λ is decreasing, with decreasing cluster size. Consequently, we anticipate the phase transition to be completely washed out in clusters of about 20 atoms or less. It will be interesting to pursue the study of superfluid densities as a function of temperature for a series of small clusters, to see if some of these clusters are indeed non-superfluid even at 0 K.

20.4 Detecting Superfluidity

Two research groups have been making pioneering efforts to detect superfluidity in free helium clusters, but the experimental evidence so far is inconclusive.^[15, 16] This stems primarily

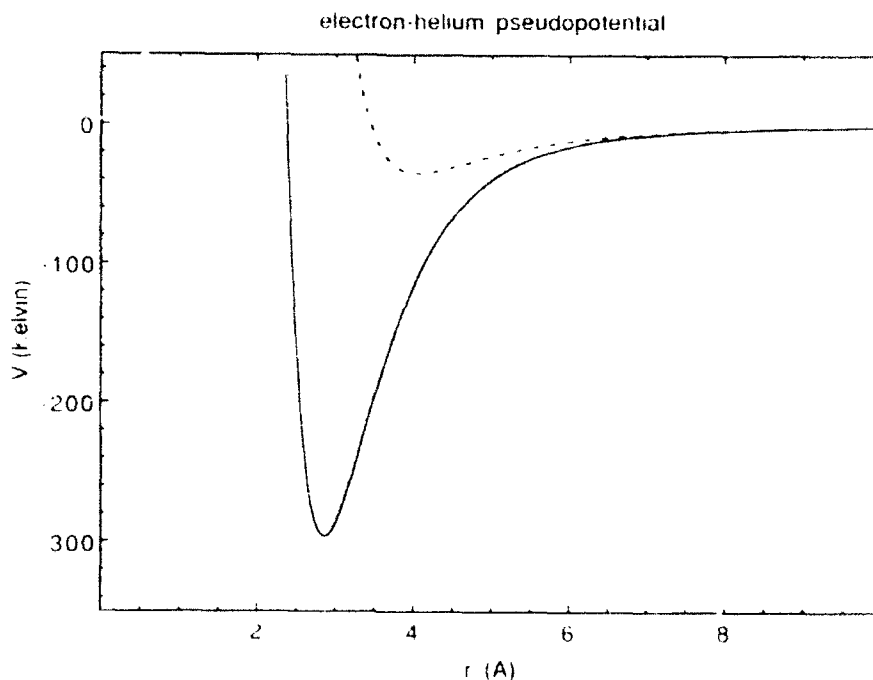


Figure 20.2: New electron-He pseudopotential of Ref. 18 (—) is compared with the best previous potential, Ref. 19 (----).

from the difficulty in probing these extremely weakly bound van der Waals clusters, which are easily dissociated and whose internal excitations have until now been poorly understood. Heat capacity measurements^[17] on bubbles of helium confined in copper foil have shown presence of the superfluid state in bubbles of radius 40–60 Å, corresponding to $N \geq 10^4$. These experiments provide direct evidence for the depression of T_λ and rounding of the heat capacity peak in these finite systems, although quantitative analysis of T_λ is complicated by the presence of the confining copper matrix.

The possibility of binding an electron to the surface of helium clusters was considered recently, in order to use it as a spectroscopic probe of the cluster. A simple but accurate electron-He interaction potential (pseudopotential) capable of reproducing s- and p-wave scattering phase shifts accurately over a range of energies is needed as a start. Such a pseudopotential has only recently been developed.^[18] In Fig. 20.2, it is compared with the commonly used prior pseudopotential for this system.^[19] The well depth of about 300 K is almost ten times deeper than the previous pseudopotential. The phase shifts and scattering cross sections calculated using this new pseudopotential are given in Table 20.2. These reproduce s- and p-wave scattering phase shifts to within 1.5%, and total and momentum-transfer cross sections to within 3% of the exact values,^[20] over a range of electron energies from 0–16 eV. This is a major improvement over the previous pseudopotential, which gives s-wave phase shifts to within only 38%, and yields p-wave phase shifts with an incorrect sign.

Using this very accurate pseudopotential for the short-range interaction, and a polarization

Table 20.2: Phase shifts and cross sections calculated using the new pseudopotential. The % errors given in the parentheses are calculated using the estimated values given in Tables III and IX of Ref. 20. The total and momentum-transfer cross sections are obtained from the s- and p-wave phase shifts calculated using the e-He_N pseudopotential of Ref. 18 and Eqs. (7) and (10)–(12) of Ref. 20.

E(eV)	Phase Shifts (radians)		Cross Sections ($\times 10^{-16} \text{ cm}^2$)	
	s-wave	p-wave	Total	Momentum transfer
0.136	-0.12700 (-0.9)	0.00311 (0.9)	5.656 (-1.8)	5.929 (-1.8)
0.544	-0.26581 (0.1)	0.01318 (0.5)	6.118 (0.2)	6.695 (0.3)
1.224	-0.40785 (1.4)	0.03069 (0.2)	6.265 (2.7)	7.107 (2.5)
2.177	-0.54667 (1.5)	0.05526 (0.1)	6.151 (2.6)	7.157 (2.3)
3.401	-0.67824 (1.5)	0.08572 (-0.4)	5.860 (2.3)	6.898 (2.0)
4.898	-0.80070 (1.0)	0.12035 (-0.4)	5.473 (1.3)	6.417 (1.0)
6.666	-0.91352 (0.8)	0.15719 (-1.0)	5.047 (0.7)	5.802 (0.4)
8.707	-1.01691 (0.1)	0.19439 (-0.8)	4.616 (-0.0)	5.131 (-0.6)
11.020	-1.11137 (-0.4)	0.23043 (-0.0)	4.200 (-0.4)	4.460 (-0.2)
13.605	-1.19750 (-0.7)	0.26422 (0.6)	3.808 (-0.3)	3.830 (0.0)
16.462	-1.27604 (-0.7)	0.29508 (0.6)	3.445 (-0.1)	3.261 (0.1)

potential for the long-range, we obtain a complete e-He_N potential.^[18] The energy levels of the excess electron may now be determined for clusters of various sizes. One of the interesting results of this calculation is that it takes approximately 5×10^5 helium atoms to barely bind the electron with a binding energy of about 0.04 cm^{-1} . Also, the electron is very “diffusely” bound to the clusters (see Fig. 20.3), which unfortunately makes it insensitive to the internal structure and dynamics of the clusters. When the cluster is large enough to be considered bulk liquid helium, the experimental zero-field energy levels of the excess electron are reproduced.^[18] This gives us confidence in the accuracy of the pseudopotential and also in the calculated energy levels of the excess electron on clusters. While it is possible in principle to determine the sizes of the large clusters by comparing the experimental and theoretical values of the energy of the photon needed to barely detach the excess electron, the very weak binding does not make this a very useful probe. We are investigating the use of embedded molecules as alternative indirect spectroscopic probes of the cluster size and dynamics. Moreover, the accurate electron-He_N pseudopotential now available makes it possible to model e-He_N scattering experiments, which could possibly provide insight into ways to excite the collective states of the cluster, and thereby yield experimental confirmation of the calculated excitation spectrum.

20.5 Summary

Theoretical evidence has been presented for the existence of superfluid helium clusters at experimentally accessible temperatures. Large clusters of several hundred atoms appear to undergo a transition to a superfluid state strongly resembling that of bulk liquid helium. Exper-

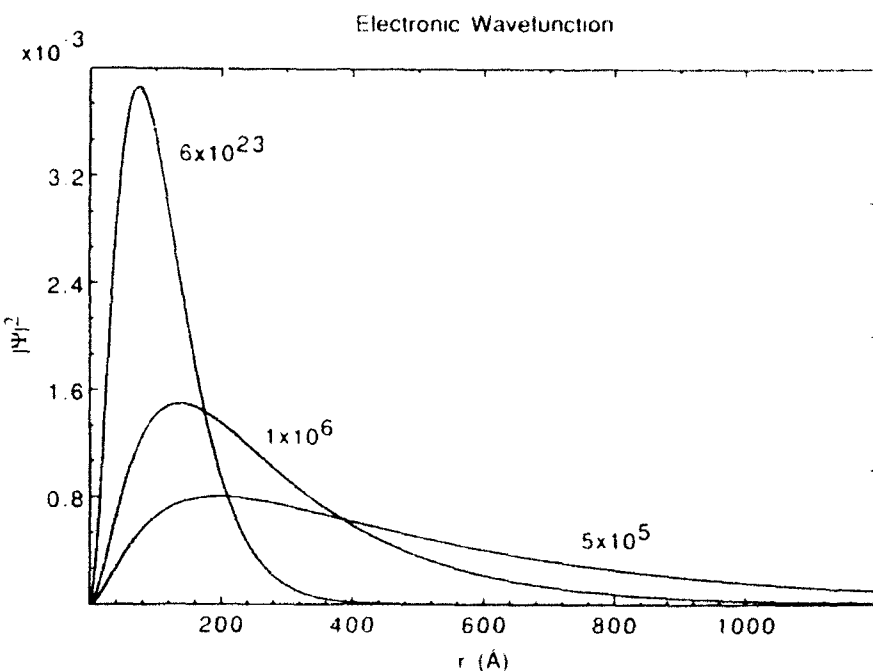


Figure 20.3: The square of the wavefunction of an excess electron attached to the surface of various He_N clusters, versus the distance r from the cluster. The cluster size N is indicated on the plots.

imental detection of such a superfluid state remains an outstanding problem. Theoretically, it remains to be investigated whether small clusters with $N < 20$ will be superfluid in any sense at any temperature, and what atomic motions are responsible for the superfluid dynamics. Theoretical efforts are also necessary to determine the best possible experimental means of detecting superfluid behavior in these extremely weakly bound clusters.

Acknowledgements

This work is supported by the Office of Naval Research. RK is grateful to IBM for the award of a Postdoctoral Fellowship.

References

1. R. P. Feynman, *Statistical Mechanics* (Benjamin, Reading, Massachusetts, 1972); J. Wilks and D. S. Betts, *An Introduction to Liquid Helium* (Clarendon Press, Oxford, 1987).
2. C. Kittel and H. Kroemer, *Thermal Physics* (W. H. Freeman, San Francisco, 1980).

3. S. Eliezer, A. K. Ghatak, and H. Hora, *An Introduction to Equations of State: Theory and Applications* (Cambridge University Press, Cambridge, 1986).
4. V. R. Pandharipande, J. G. Zabolitzky, S. C. Pieper, R. B. Wiringa and U. Helmbrecht, *Phys. Rev. Lett.* **50**, 1676 (1983).
5. V. L. Ginzburg and L. P. Pitaevskii, *J. Exptl. Theoret. Phys. (USSR)* **34**, 1240 (1958) [*Sov. Phys. JETP* **34**, 858 (1958)].
6. Yu. G. Mamaladze, *Zh. Eksp. Teor. Fiz.* **52**, 729 (1967) [*Sov. Phys. JETP* **25**, 479 (1967)]; *Phys. Lett.* **27A**, 322 (1968).
7. V. L. Ginzburg and A. A. Sobyanin, *Usp. Fiz. Nauk* **120**, 153 (1976) [*Sov. Phys. Usp.* **19**, 773 (1976)].
8. V. L. Ginzburg and A. A. Sobyanin, *J. Low Temp. Phys.* **49**, 507 (1982); L. V. Kiknadze and Yu. G. Mamaladze, *Fiz. Nizk. Temp.* **2**, 413 (1976) [*Sov. J. Low Temp. Phys.* **2**, 205 (1976)].
9. A. A. Abrikosov, L. P. Gorkov and I. E. Dzyaloshinski, *Methods of Quantum Field Theory in Statistical Physics*, (Dover, New York, 1975).
10. M. V. Rama Krishna and K. B. Whaley, *Phys. Rev. Lett.* **64**, 1126 (1990).
11. M. V. Rama Krishna and K. B. Whaley, *J. Chem. Phys.* **93**, 746, 6738 (1990).
12. N. N. Bogoliubov, *J. Phys. USSR* **11**, 23 (1947).
13. M. A. Ricci, D. Rocca, G. Ruocco and R. Vallauri, *Phys. Rev. Lett.* **61**, 1958 (1988).
14. P. Sindzingre, M. L. Klein and D. M. Ceperley, *Phys. Rev. Lett.* **63**, 1601 (1989).
15. H. Buchenau, R. Götting, A. Scheidemann and J. P. Toennies, in *Proceedings of the 15th Int'l Symp. on Rarefied Gas Dynamics*, Vol. 2, V. Boffi and C. Cercignani, eds., (Tuebner, Stuttgart, 1986); J. P. Toennies, in *Proceedings of the 107th Course of the Int'l School of Physics "Enrico Fermi" on the Chemical Physics of Atomic and Molecular Clusters*, (Societa Italiana di Fisica, 1988); D. Eichenauer, A. Scheidemann and J. P. Toennies, *Z. Phys. D* **8**, 295 (1988).
16. J. Gspann, *Physica B* **108**, 1309 (1981); J. Gspann and R. Ries, *Surface Science* **156**, 195 (1985); J. Gspann and R. Ries, in *Physics and Chemistry of Small Clusters*, P. Jena, B. K. Rao and S. N. Khanna, eds. (Plenum, New York, 1986).
17. E. G. Syskakis, F. Pobell and H. Ullmaier, *Phys. Rev. Lett.* **55**, 2964 (1985).
18. M. V. Rama Krishna and K. B. Whaley, *Phys. Rev. B* **38**, 11839 (1988).
19. D. F. Coker, B. J. Berne and D. Thirumalai, *J. Chem. Phys.* **86**, 5689 (1987).
20. R. K. Nesbet, *Phys. Rev. A* **20**, 58 (1979).

Monte Carlo study of impurities in quantum clusters: H_2 - 4He_N , $N=2-19$

R. N. Barnett and K. B. Whaley

Department of Chemistry, University of California, Berkeley, California 94720

(Received 21 June 1991; accepted 29 October 1991)

Variational Monte Carlo techniques are employed in studying 4He clusters, with and without an H_2 impurity. We find that a novel, yet simple, analytic nuclear wave-function form, derived from a numerical H_2 -He wave function, yields high accuracy in computed ground-state energies of 4He_N . For the clusters studied here, three to twenty atoms, energies range from 94% to 90% of the exact values. Density profiles and distributions of particle separation are also computed. For reasonable computational cost (e.g., < 20 Cray/X-MP14 minutes for the largest cluster), density profiles are determined for the first time to high statistical accuracy to within 0.5 Å or less of the cluster center. The density profile of He, is found to possess a uniquely pronounced peak at the cluster center resulting from contributions of near-collinear atomic arrangements. We also study the effect of substituting an He by H_2 , using modified wave functions containing products of pairwise He- H_2 terms. For all cluster sizes studied, we find a lowering of the total energy upon exchanging an He for an H_2 . The exchange energy increases in magnitude with increasing cluster size, yet is still well below bulk estimates at $N = 20$. Size comparisons with the pure helium clusters show very little change upon He/ H_2 exchange, e.g., the rms radii differ by <2% for $N > 3$. Density profiles and bond distributions show noticeable differentiation between H_2 and He. For $N > 4$, the peak in the H_2 density profile is not at the cluster but does remain inside the cluster. This peak is most pronounced for H_2 - He_{13} , implying an enhanced resistance to H_2 penetration for He_{13} .

I. INTRODUCTION

Clusters of rare gases constitute the simplest van der Waals aggregates. These species continue to provide much stimulus for both experimental and theoretical investigation of size-dependent properties in the regime spanning molecular and bulk systems.¹ Theoretical study is especially attractive because the interaction potentials are so well known. The most weakly bound of these species is 4He_N , in which large quantum effects are apparent, making them of special fundamental interest for the understanding of size-dependent behavior of quantum systems. Recent predictions for these Bose clusters, based upon scaling of the microscopic excitation spectra² and the calculation of the phenomenologically defined superfluid fraction,³ has for the first time provided a quantum analog to recent extensive analysis of phase transitions and structural features of classical clusters.⁴

While these weakly bound species intrinsically provide ideal testing grounds for new theoretical approaches to large quantum aggregates, contact with experimental studies has thus far proved elusive. The ease of dissociation and the liquidlike structure of helium clusters, which facilitates the absorption of foreign species, has also rendered the results of scattering experiments ambiguous.^{5,6} Nevertheless, there does now exist a considerable body of experimental data on the pickup abilities and ionization patterns.⁶ It has become clear that rather than attempting a direct probe of the dynamics and excitations of these quantum clusters, indirect probes via spectroscopic studies of embedded species, preferably without the additional complications introduced by dissociation channels, will provide more useful information. Infrared spectroscopy of small molecules in argon clusters has

yielded information on the location of the foreign species.⁷ The same information is, in principle, available for the quantum clusters of helium, and furthermore, analysis of spectroscopic line shapes should give information on the coupling to the internal cluster excitations and whether these are collective or single-particle-like.

In this paper we undertake a fully quantum-mechanical study of an embedded molecule in helium clusters. We employ variational Monte Carlo (VMC) methods in studying the structural and energetic effects of adding a foreign species, using a new wave-function form based on accurate pair potentials. The techniques are applied here to H_2 in He_N (from here on 4He_N is assumed), a choice motivated by both the availability of high-quality He-He and H_2 -He potentials, and also by prior experimental observations of H_2 in bulk helium.⁸ We calculate the ground-state energy of clusters with $N < 20$, with and without an H_2 species attached, and thereby the He/ H_2 exchange energy. Analysis of the density profiles resulting from the optimized wave functions shows that the embedded H_2 is extensively delocalized throughout the cluster, with a small peak in the concentration beneath the surface. Such structural analysis clearly describes the location of the foreign species.

Very few species are even metastable in bulk helium because of its closed-shell configuration and inert nature. However, there has been continued interest in the analysis of impurities in bulk helium because of the properties of these both as nucleation centers,⁹ and as a source of information on the induced response and spatial structure of the bulk medium. The only theoretical work to date for species other than the isotopic impurity 3He has employed paired phonon analysis in the hypernetted-chain approximation with Lennard-Jones potentials.¹⁰ As pointed out by Kürten and Ris-

ting in Ref. 10, these techniques are subject to large errors. However, it has proven difficult to proceed beyond this level of description, either by VMC or Green's function Monte Carlo (GFMC), because of the relatively small contribution of the impurity to the total energy in the bulk system. Analysis of the cluster energies with and without impurities as a function of cluster size provides a means of approaching the bulk impurity problem by extrapolation, and therefore yields a new microscopic approach to the impurity probe problem for bulk helium as well as for clusters.

The energies computed here for the pure He_N clusters compare favorably with previous VMC and obtain a high percentage of the exact diffusion Monte Carlo (DMC) energies. In our wave functions only two-body correlation factors are used. One-body factors, often employed in cluster calculations, are not found to be necessary here, and three-body factors are seen to become significant only for $N \geq 20$. Details of the physical motivation of our wave-function form and a thorough description of the various Monte Carlo approaches employed are presented elsewhere.¹¹ The remainder of this paper is organized as follows. Section II contains a description of our theoretical approach, with a brief summary of the guided and unguided Metropolis walks used here, in addition to description of the potentials, wave-function forms, and optimization. Results for pure and mixed clusters are presented and discussed in Sec. III. Conclusions, together with a prognosis for further studies of excitations and dynamics of clusters with foreign species, are presented in Sec. IV.

II. THEORETICAL APPROACH

The quantum ground states are studied by seeking accurate many-body nuclear wave functions. That is, in place of unknown eigenfunctions of the nuclear Schrödinger equation, we obtain wave functions for which the energy $E = \langle \Psi | H | \Psi \rangle / \langle \Psi | \Psi \rangle$ is minimized. For the systems we treat here, the Hamiltonian H is, in atomic units,

$$H = - \sum_i (2m_i)^{-1} \nabla_i^2 + \sum_{i < j} V_{ij}, \quad (1)$$

where a pairwise potential is considered sufficient for weakly interacting clusters.¹²

For the pure He clusters $m_i = m_{\text{He}}$ and $V_{ij} = V$ is the accurate and widely employed interatomic potential determined by Aziz, McCourt, and Wong in 1987.¹³ This potential has a slightly deeper well than the previous one determined in 1979,¹⁴ and yields a bound state for the He-He dimer at $\sim 10^{-3}$ K. For clusters containing H_2 , vibration of the foreign molecule is neglected. This should be quite reasonable for these weakly bound clusters since the vibrational dependence of the H_2 -He potential is significant only at small separations R (R is the distance from the H_2 center of mass to He). In addition, the H_2 -He potential is very nearly isotropic.¹⁵ Expanding $V_{\text{H}_2\text{-He}}(R, \theta)$ in the Legendre polynomials $P_0(\cos \theta)$ and $P_2(\cos \theta)$ (θ is the angle between the intermolecular axis and \mathbf{R}) yields an anisotropic component $V_2(R)$ with a well depth an order of magnitude smaller than that of $V_0(R)$. Therefore, as a further yet still accurate approximation, we choose $V_{\text{H}_2\text{-He}} = V_0$. Thus, in the Hamil-

tonian we employ, H_2 acts as a single particle with twice the He-atom mass and interacts with He via V_0 .

The potential V_0 is a Lennard-Jones plus van der Waals fit to the *ab initio* data of Ref. 15.

$$V_0(R) = \begin{cases} 4\epsilon[(\sigma/R)^{12} - (\sigma/R)^6], & R < R_c, \\ -C_6R^{-6} - C_8R^{-8} - C_{10}R^{-10}, & R > R_c, \end{cases} \quad (2)$$

where R_c is chosen such that the two forms in Eq. (2) take essentially the same value at this point. The van der Waals parameters are taken from Ref. 15. Table I lists the parameters describing V_0 and Fig. 1 compares V_0 with the *ab initio* data points (the root-mean-square deviation is 1.9%), and with the He-He potential.

A. Wave-function form and optimization

Once a wave-function form is chosen, parameters are varied to minimize the energy, E . Here, Ψ takes a translationally invariant product form,

$$\Psi(\mathbf{R}) = \prod_{i,j} \psi_{ij}(r_{ij}), \quad (3)$$

where for N particles, \mathbf{R} is a $3N$ -dimensional vector specifying the particle locations, and $r_{ij} = |\mathbf{r}_i - \mathbf{r}_j|$. The function ψ_{ij} , analogous to the f_2 factor defined in previous studies of atomic clusters,^{2,16-18} varies with differing particle pairs, i.e., He-He or H_2 -He. Note that a one-body factor $f_1(\mathbf{r}_i)$ is not employed. Such a factor introduces undesired center-of-mass motion. In this event, the associated translational energy must be subtracted (unless N is large), adding to computational cost. Alternatively, translational invariance may be maintained by replacing \mathbf{r}_i by $\mathbf{r}_i - \mathbf{R}_{\text{c.m.}}$, where $\mathbf{R}_{\text{c.m.}}$ is the center-of-mass vector, yielding a sum of interparticle separations. In this case, therefore, f_1 is actually a many-body factor. A common motivation for including f_1 is its use in binding the cluster and in describing the more diffuse regions. Since our two-body factor is derived from an exact dimer (H_2 -He) wave function, in which particular attention is paid to the long-range, diffuse tail, part of the wave function,¹¹ we prefer not to modify this by addition of a one-body retaining factor. If the cluster is bound, this should be reproduced by a pairwise wave function, provided it is of sufficiently high accuracy. Our new approach differs from the original one of Pandharipande, Pieper, and Wiringa,¹⁶ which constrained the asymptotic form of ψ_{ij} by the relation between the pair distribution function $g(r)$ and the speed of sound in the bulk system, thereby necessitating a one-body factor to yield a bound finite system. Therefore, although a one-body factor

TABLE I. Parameters of the H_2 -He interaction potential, V_0 , Eq. (2)

Parameter	Value	Units
$10^3\epsilon$	4 189 712	hartrees (\hbar)
σ	5.671 145	Bohr
R_c	8.351 10	Bohr
C_6	4.018	\hbar (Bohr) ⁶
C_8	55.69	\hbar (Bohr) ⁸
C_{10}	1 031.0	\hbar (Bohr) ¹⁰

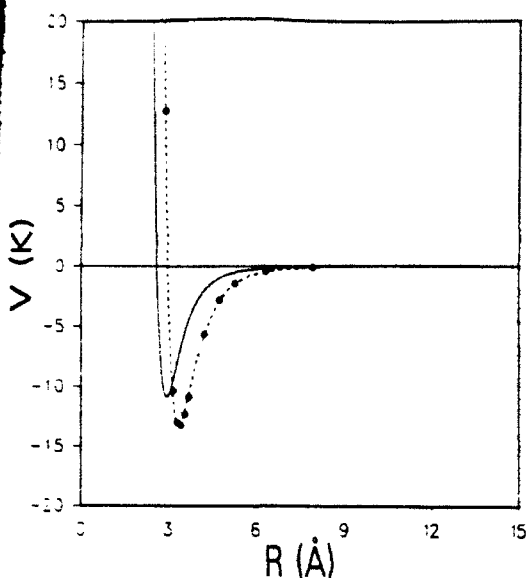


FIG. 1. H₂-He and He-He potentials. The solid line shows the He-He potential of Ref. 13, and the dotted line shows the H₂-He potential, V_0 , Eq. (2) and Table I. The *ab initio* data points for V_0 , given in Ref. 15, are indicated by the solid circles.

has proved useful in earlier studies, it is extraneous for our purposes. We also do not employ a three-body factor here because of the high-quality wave functions we obtain at the two-body level of wave-function complexity. We shall refer to this point again in Sec. III. The factors ψ_i are

$$\psi_i(r) = r^a \exp\{P(u) + ar^\alpha\}, \quad (4)$$

$$P(u) = \sum_{k=0}^5 a_k u^k, \quad u = r^{-1}. \quad (5)$$

The ij subscripts are omitted from the parameters for convenience; however, parameters describing different interactions, i.e., V and V_0 , are independent. This form was deduced from the numerical solution to the Schrödinger equation employing the H₂-He potential given in Eq. (2).¹¹

The wave-function form may now be considered as the product of a long-range and a short-range factor. At large interparticle separations where the polynomial P is roughly constant, the behavior of ψ is determined by a , b , and α . The long-range factor, $r^a \exp(ar^\alpha)$, is very similar to that employed in previous work,^{2,16-18} with the exception that α is now a variable parameter which when optimized for our wave functions is different from unity. Note that for $b = -(N-1)^{-1}$ and $\alpha = 1$, our form reduces to the one-parameter model asymptotic form for a two-fragment bound system.¹⁹ The remaining factor, $\exp\{P(u)\}$, is most important at small separations and can be considered as a generalization of the McMillan form used for bulk He.²⁰ Given the highly repulsive behavior of the potential at small particle separations, an increase in wave-function complexity for describing the short-range interactions should be especially useful. We therefore include *all* integer powers up to five in P . The study of a further improved two-body form, which yields an entirely new description of the behavior at small particle separations tailored to the functional form of the

repulsive part of the potential, will be considered in another work.¹¹

The major motivation in employing such wave functions is our belief that considerable improvement over previous two-body forms can be made, to the extent that one can efficiently obtain high accuracy without the use of a complex three-body factor. The general questions of what accuracy is achievable at the two-body level of theory and the extent to which our wave functions obtain this accuracy are addressed in a subsequent publication.¹¹ A second motivation for producing such accurate wave functions is the need for high accuracy when considering a weakly bound impurity species.

Below we outline our wave-function optimization approach. Full details are given in Ref. 11. We optimize the parameters by minimizing fluctuations of the local energy, $E_L \equiv \Psi^{-1} H \Psi$, about a reference (or guess) energy, E_R , over a fixed set of points in the 3N-dimensional space \mathbf{R} . The quantity of interest is then

$$s^2 = \frac{\sum_{i=1}^N [E_L(\mathbf{R}_i) - E_R]^2 |\Psi(\mathbf{R}_i)/\Psi_0(\mathbf{R}_i)|^2}{\sum_{i=1}^N |\Psi(\mathbf{R}_i)/\Psi_0(\mathbf{R}_i)|^2} - \frac{\langle \Psi | [H - E_R]^2 | \Psi \rangle}{\langle \Psi | \Psi \rangle}, \quad (6)$$

where the second equation corresponds to an infinite number of points sampled from $|\Psi_0|^2$. The essence of this "fixed-sample" approach²¹ is that multidimensional integrals are approximated as summations over points in a distribution corresponding to an initial (unoptimized) wave function, Ψ_0 . Parameters are converged to optimum values (in a local minimum sense) with a conjugate gradient technique.²²

The reference energy E_R determines the emphasis given to minimizing the energy vs minimizing the variance. If $E_R \ll \bar{E}_L$, minimizing s^2 is equivalent to minimizing the average local energy, where

$$\bar{E}_L = \frac{\sum_{i=1}^N E_L(\mathbf{R}_i) |\Psi(\mathbf{R}_i)/\Psi_0(\mathbf{R}_i)|^2}{\sum_{i=1}^N |\Psi(\mathbf{R}_i)/\Psi_0(\mathbf{R}_i)|^2} - \frac{\langle \Psi | H | \Psi \rangle}{\langle \Psi | \Psi \rangle}. \quad (7)$$

However, if $E_R = \bar{E}_L$, then minimizing s^2 is equivalent to minimizing the variance in the energy. Correspondingly, choosing intermediate values of E_R mixes energy and variance reduction. As we are primarily interested in obtaining the lowest-energy wave functions possible, we generally choose the reference energy to be much lower than \bar{E}_L .

Since N is finite (< 5000 points), the summations in Eq. (6) may be poor approximations to the desired expectation value. This is especially true when Ψ becomes much different than Ψ_0 , which occurs if Ψ_0 is a poor initial guess. Therefore, we have found it useful to set $\Psi_0 = \Psi$ and to generate a new ensemble from the updated Ψ_0 . The conjugate gradient minimization is then continued. This updating procedure greatly enhances the reliability of the degree of energy minimization indicated by an individual fixed-sample optimization. Generally, one or two updatings have proved suffi-

cient to obtain stable and converged results. The optimized wave-function parameters are given in the Appendix.

B. Monte Carlo approach

We are interested in computing expectation values of Ψ , which cannot be done analytically. Numerical quadrature may be employed but, given the high dimensionality involved here, Monte Carlo integration is the most tractable approach. Here, we employ two variants of the Metropolis walk.²³ The first is the commonly used "unguided" walk by which points are sampled from $|\Psi|^2$. Here, unguided refers to the fact that the attempted moves underlying the walk are completely random. Expectation values are computed, to within statistical error, as

$$\bar{A} = N^{-1} \sum_{i=1}^N A(\mathbf{R}_i) - \langle \Psi | A | \Psi \rangle / \langle \Psi | \Psi \rangle. \quad (8)$$

All previous VMC cluster studies employed unguided walks.^{2,16-18} The second approach used here employs a walk guided by a different function, Ψ_g . For these walks, attempted moves are biased towards larger values of the sampled distribution, $|\Psi_g|^2$. (Walks guided by Ψ itself yielded poor convergence at small particle separations.¹¹) Expectation values with respect to Ψ now require a weighting procedure, namely,

$$\bar{A}_g = \sum_{i=1}^N A(\mathbf{R}_i) |\Psi(\mathbf{R}_i)/\Psi_g(\mathbf{R}_i)|^2 \times \left[\sum_{i=1}^N |\Psi(\mathbf{R}_i)/\Psi_g(\mathbf{R}_i)|^2 \right]^{-1}. \quad (9)$$

Generally, the usefulness of a guided walk arises from importance sampling, i.e., the preferential sampling of (important) regions where good statistics are required for high precision in \bar{A}_g . Here, $\Psi_g \approx \Psi$ is chosen so that $|\Psi|^2$ is preferentially sampled in regions where it is large. The guiding function is also chosen to decay to zero more slowly than Ψ at small r to facilitate convergence in this domain, where significant contributions to the energy are typical. A particular advantage of the "guided/weighted" walk lies in the flexibility of choosing which regions are to be emphasized. For example, if high precision is desired at small separations, choosing $|\Psi_g/\Psi| > 1$ in this domain yields the desired sampling. The guided/weighted walk was most useful for the smaller clusters studied here. Detailed comparisons of the various walks and their relative merits for these weakly bound systems are presented in Ref. 11.

As a final point, we discuss the evaluation of statistical error. The primary concern is that averaged quantities be statistically independent so that the computed statistical error is unbiased. In our approach this is accomplished by propagating (ten) independent ensembles of (100) points $\{\mathbf{R}_i\}$ yielding (ten) independent Monte Carlo estimates. Ideally, this can be accomplished by a random selection of points. In practice, for the smallest clusters, the ensembles are not initially decorrelated but commence with different random number seeds. The ensembles are propagated in parallel by a Monte Carlo walk until decorrelation between them is obtained. Decorrelation may be ascertained from the stability of the statistical error in the average of the (ten)

Monte Carlo estimates. Also, if the distance moved in configuration space by each member of all the ensembles is several times larger than the dimensionality of the cluster, then the ensembles can be assumed to be decorrelated. To reduce this initial decorrelation time, ensembles for larger clusters are built up from the ensembles of the next smallest cluster. In addition, this parallel structure is also maintained when generating large ensembles of points by VMC walks during wave-function optimization. Given that each ensemble is different from the others, employing these ensembles in Monte Carlo runs yields a set of independent results. This enables the computation of an unbiased statistical error. This method of evaluation of the statistical error is used for all expectation values, including those yielding distribution functions such as density profiles.

III. RESULTS AND DISCUSSION

A. Pure He_N

In this work we study clusters ranging in size from three to twenty particles, the focus being the ground-state energy and structure. The primary concern here is wave-function accuracy, as measured by the energies obtained. Therefore, we first compare our pure He cluster energies with those resulting from other (sometimes more complex) wave functions and with new DMC energies which are exact.

Table II compares our optimized He cluster energies obtained with the new wave function, Eqs. (3)–(5), with those resulting from other work. Exact energies, from which percent accuracies are obtained, are the DMC values given in Ref. 11. For $N = 3–5$, we see that our computed energies lie below previous VMC values which were computed employing both one- and two-body factors, indicating the high quality obtainable with our two-body wave functions for these small clusters. Similar accuracy has also been obtained with two-body wave functions for $N = 3–7$.²⁴ For He₁₀, our new energy reproduces to within the statistical error (given in parentheses) our previous result obtained with one-, two-

TABLE II. He cluster per particle energies.*

This work		Previous VMC	
–E/N (K)	% of Exact	–E/N (K)	% of Exact
He ₃ –0.0415(1)	93.9	–0.0388(9) ^b	87.7
He ₄ –0.1357(1)	93.9	–0.1320(10) ^b	91.3
He ₅ –0.2505(2)	93.5	–0.128 ^c	96.0 ^d
He ₆ –0.4838(1)	92.7	–0.2440(10) ^b	91.1
He ₁₁ –1.0545(6)
He ₁₄ –1.1290(7)	90.5
He ₂₀ –1.510(2)	89.5	–1.514(3) ^b	89.7
		–1.573(1) ^c	96.7 ^d

* Here and in Table III, the statistical error representing one standard deviation in the mean is shown in parentheses. Exact energies for the most recent potential are computed by DMC in Ref. 11.

^b Reference 18.

^c Reference 16.

^d Since Ref. 16 employs the previous potential of Ref. 14, the exact energy is taken to be the GFMC value of Ref. 25.

and three-body factors, and gives 89.5% of the exact DMC energy. (This is somewhat less accurate than the VMC result of Pandharipande, Pieper, and Wiringa,¹⁶ also obtained with one-, two-, and three-body factors, for the earlier potential,¹⁴ which yielded 96.7% of the exact GFMC energy.²³) Given the simplicity of our wave function, the proximity of our energy to that resulting from one which is more complex is quite satisfying. However, we see that for very high accuracy, three- and perhaps higher-body factors are required for $N \geq 20$. In this case, our present wave functions appear to provide a two-body component of high quality.

Overall, Table II shows that the accuracy of our energies, vis-à-vis those of DMC, decreases with increasing cluster size. Naturally, this is expected as a pure "two-body" wave function should be less appropriate as the importance of three-body and more complex interactions increase, as is the case for larger clusters. However, it is pleasing to see that, despite the constant level of wave-function complexity, the (energy) accuracy does not degrade rapidly. As the cluster size increases from 7 to 20 atoms, the amount of the DMC energy obtained decreases by only 3%. In addition, the total accuracy remains good up to $N = 20$, with 90% of the DMC energy obtained for this cluster. Therefore, the wave-function form employed here is considered to be of sufficiently high flexibility for the study of the H_2 , He_N clusters, $N < 19$.

Helium cluster density profiles are presented in Fig. 2. The data were obtained by binning the sampled points into bins corresponding to $\Delta R < 0.03 \text{ \AA}$. Note that the bin volume and therefore the statistical precision decrease as the cluster center is approached, as indicated by the fluctuations in ρ which well represent statistical error. In spite of this, precision remains high up to small distances from the cluster center. For He_{20} , for which uncertainty in ρ is greatest, the computed statistical error in each bin is under 5% from 0.5 to 12 \AA . Thus, any peculiar behavior at the cluster center, such as

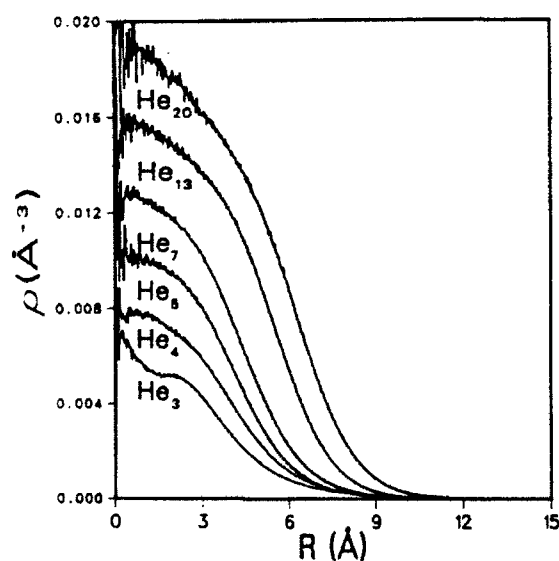


FIG. 2. Helium density profiles for pure helium cluster sizes $N = 3-5, 7, 13, 20$. The bin size is $< 0.03 \text{ \AA}$.

a hole, as well as any hard-core structure in the single-particle distribution function, is mostly precluded by our data. The computational cost of the He calculations presented here is very reasonable, ranging from 4 Cray/X-MP14 minutes for He_3 , to 19 CPU minutes for He_{20} . These profiles represent the first Monte Carlo study of any type, VMC, GFMC, or DMC, which possess this high level of statistical accuracy in the interior of the clusters. As reflected in Fig. 2, the efficiency of computing density profiles decreases with increasing cluster size. For a cluster with N particles, each point sampled yields N values to be binned. However, the computational cost increases as N^2 , causing the efficiency for this quantity to scale as N^{-1} .

Figure 2 demonstrates the unique character of the He_3 density profile. Approaching the cluster center, the He_3 profile is similar in character to those of the other clusters up to the shoulder located at about 2.2 \AA . After this point, a marked change in behavior occurs as ρ increases only slightly from about 2.2 \AA to 1 \AA , and then rises rapidly closer in. These characteristics are presented in greater detail in Fig. 3. In addition to the density profile, contributions to ρ are presented conditional on the largest angle (θ_{\max}) in the He_3 triangle being greater than 120°, 140°, and 160°. This figure shows that the rapid rise in ρ near the origin is due solely to near-collinear arrangements starting at $\theta_{\max} \approx 120^\circ$. That density near the center arises solely from near-collinear arrangements is not unreasonable given the high potential energy for atoms near the cluster center (and each other) in a near-equilateral configuration. However, the rapid increase in ρ caused by a tendency towards collinearity is interesting given the large difference of a collinear structure from that of

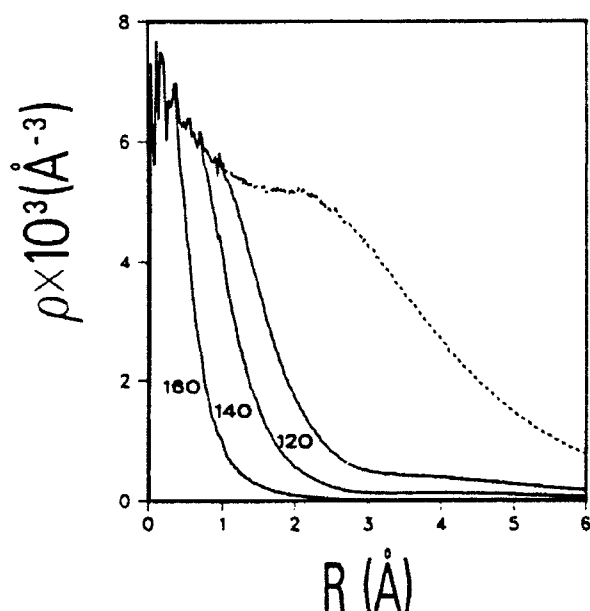


FIG. 3. Conditional density profiles of He_3 . The dashed line is the density profile. The three conditional density profiles, solid lines, are obtained by binning distances from the cluster center only when the atomic arrangement sampled possesses an angle greater than 120°, 140°, and 160°.

minimum potential energy, an equilateral triangle.

In addition to the density profiles, we present particle separation probability density functions $p(r)$ (normalized such that $\int p(r)dr = 1$) in Figs. 4 and 5. These plots were obtained by binning particle separations with a bin size $\Delta r < 0.03 \text{ \AA}$. The curves in Fig. 4 show a trend toward decreasing diffuseness as the cluster size increases from three to five atoms, consistent with increasing density and also increasing binding energy per particle. Upon considering the larger clusters (Fig. 5) this trend reverses. The interparticle separations increase slightly from He_3 to He_7 and more noticeably upon going to He_{13} and He_{20} . The He_N root-mean-square (rms) radii presented in Table IV mirror this behavior, which has been previously noted by Pandharipande, Pieper, and Wiringa.¹⁰ What is most interesting and novel here is the appearance of structure in $p(r)$ for He_{13} and He_{20} (Fig. 5). The behavior of p as it approaches its maximum clearly differs between He_7 and He_{13} . For He_{20} the existence of a shoulder at a particle separation smaller than that corresponding to maximum p is unambiguous. However, the presence of a shoulder in p for He_{13} is less certain. The He_{14} plots of the p and ρ are virtually identical to those of He_{13} (and are, therefore, omitted for clarity). This similarity between He_{13} and He_{14} is in contrast to the larger differences between He_N and He_{N+1} observed for smaller N (Fig. 4). Therefore, given the slowly changing nature of p at $N \approx 13$, we conclude that the onset of the shoulder in p is quite gradual. Such behavior does appear to correspond to evolution of shell structure, and is related to the appearance of the second-nearest-neighbor coordination shell in the pair density distribution function $n_2(0, r)$.¹⁸ Our density functions p , together with the absence of any structure in the single-particle distribution function (Fig. 2), are consistent with the inter-

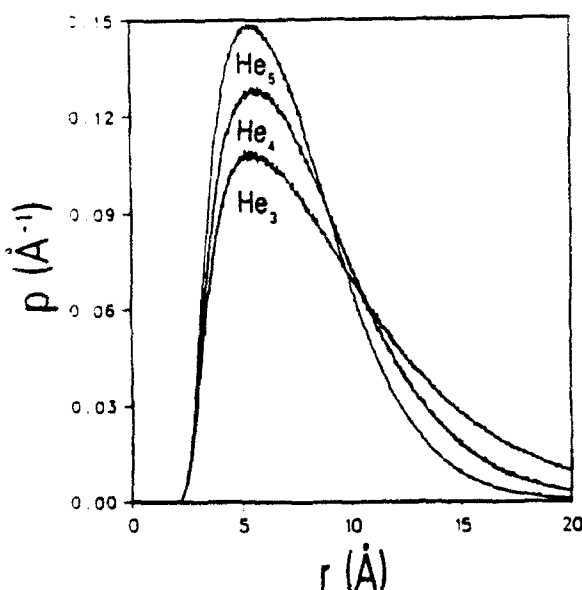


FIG. 4. Particle separation probability density function $p(r)$ for the pure helium clusters, $N = 3-5$. The function $p(r)$ is the probability density of finding any two particles separated by the distance r . The curves are normalized to unity and bin sizes are $< 0.03 \text{ \AA}$.

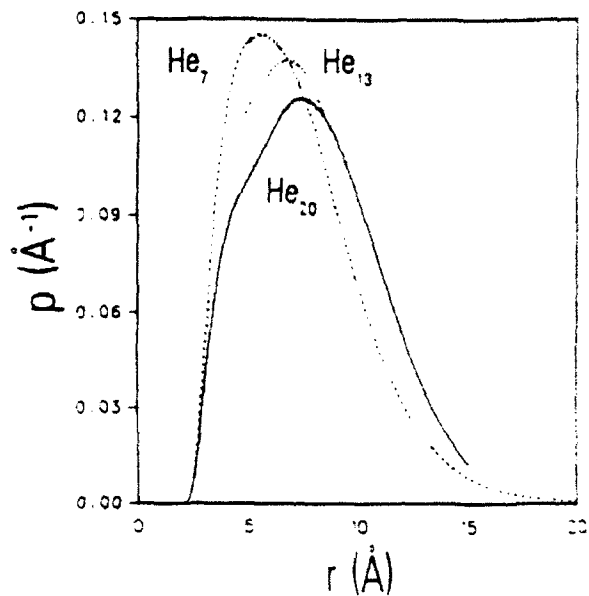


FIG. 5. Particle separation probability density function $p(r)$ for the pure helium clusters, $N = 7, 13, 20$. The normalization and bin sizes are as in Fig. 4.

pretation of He clusters as delocalized, liquidlike clusters rather than as crystalline- or molecularlike species.

B. Mixed clusters H_2He_N

Table III lists the cluster energies per particle (H_2 is considered as one particle) and the He/H_2 exchange energy as a function of size. The exchange energy (referred to as the chemical potential for He/H_2 exchange in Ref. 10) for an N -particle cluster is computed as

$$E_{\text{ex}}(N) = E(\text{H}_2\text{He}_{N-1}) - E(\text{He}_N). \quad (1)$$

For the H_2He van der Waals complex, numerical solution of the nuclear Schrödinger equation yields the ground state bound by 0.0246 K , while the He dimer is bound by only $\approx 10^{-3} \text{ K}$.¹³ This is not surprising given the greater well depth of the H_2He interaction relative to the He-He potential, cf. Fig. 1. As a consequence, negative exchange energies are observed. The exchange energy increases monotonically with increasing cluster size; however, our value at $N = 20$, $-1.68(4) \text{ K}$, is still only a fraction of Kürten and Ristic's estimate of the bulk value, -20 K .¹⁰ Table III also lists the unit radii, r_0 , defined by

$$r_0 = (\langle R^2 \rangle)^{1/2} N^{-1/3}, \quad (11)$$

where $\langle R^2 \rangle$ is the expectation value of the squared distance from the cluster center. The latter is defined as

$$R_c = \frac{1}{N} \sum_{i=1}^N \mathbf{r}_i, \quad (12)$$

i.e., the geometric center. Since the center of mass is biased towards heavier particles, we employ the geometric center as the origin in comparing structure and size of pure and mixed clusters, and, most importantly, in studying the relative location of H_2 as specified by the density profiles. Unlike the

TABLE III. Per particle energies, unit radii, and He/H_2 exchange energy.*

N	He_N		$\text{H}_2\text{He}_{N-1}$		
	E/N (K)	r_0 (Å)	E/N (K)	r_0 (Å)	E_{ex} (N) (K)
3	-0.04152(8)	5.50	-0.08938(24)	5.21	-0.1436(8)
4	-0.1357(2)	4.42	-0.2005(1)	4.51	-0.2592(9)
5	-0.2505(2)	3.76	-0.3324(2)	3.84	-0.4095(11)
7	-0.4838(1)	3.45	-0.5751(5)	3.43	-0.6391(36)
13	-1.0545(6)	2.97	-1.1461(11)	2.98	-1.191(16)
14	-1.1290(7)	2.92	-1.2242(4)	2.96	-1.333(11)
20	-1.5100(20)	2.82	-1.5943(8)	2.86	-1.680(44)

*Statistical error in r_0 is less than 0.003 Å.

per particle energies, cluster size is largely unaffected by He/H_2 exchange. As seen in Table III, the unit radii of pure and mixed clusters differ by only 4% for three particles and by 2% or less for the other clusters.

In considering the structure of the mixed clusters, in particular the degree of differentiation between H_2 and He, we first turn to the root-mean-square distance from the cluster center, $R_{rms} = (\langle R^2 \rangle)^{1/2}$. Values for He and H_2 , obtained by integrating over the density profiles shown in Figs. 6 and 7, are listed in Table IV. These density profiles, $\rho(R) = \rho(R)$, are normalized as $\int 4\pi R^2 \rho(R) dR = 1$, and as stated above the cluster center is chosen as the origin. The corresponding values for the pure clusters are also shown for purposes of comparison. As is the case for the pure clusters, we see that a minimum in cluster size, as measured by R_{rms} , also occurs at five particles for the mixed clusters. The differentiation between H_2 and He R_{rms} values within a given cluster is somewhat small but consistent. For all clusters studied here, H_2 is farther from the cluster center on average, with values of R_{rms} being 4.6% to 11% greater than those of He.

Differentiation between H_2 and He is also evident in the normalized density profiles presented in Figs. 6 and 7. To quantify this differentiation between H_2 and He, we compute the probability P of finding H_2 (or He) outside the spherical volume, centered at $R = 0$, containing half of all the particles. Values of P for both species are also listed in Table IV. These values indicate that the degree to which H_2 lies "outside" the cluster is generally not large. For all but the 14-particle cluster, 60% or less of the H_2 density lies outside the half-particle dividing radius. The exception, H_2He_{13} , for which 66% lies outside this radius, actually continues a trend from the four-particle mixed cluster which then reverses in proceeding to H_2He_{19} . This suggests a special structural robustness of He_{13} to H_2 penetration. Previous GFMC results for He argue against the presence of "magic numbers" for the pure clusters, $N < 33$.²³ However, the effect we see here is small and also may not be deducible from the energies of pure clusters. Whether the increase in penetration of H_2 seen on going to H_2He_{19} continues as N increases remains to be seen. In the bulk, H_2 penetration is observed but the extent is not known.⁸

Following the earlier discussion concerning sampling

efficiency in computing pure cluster density profiles, one finds that the efficiencies for computing the H_2 and He mixed cluster density profiles scale as N^{-2} and $(N-1)N^{-2}$, respectively. This fact is manifested by the relatively large fluctuations in the H_2 density profile as N becomes large, cf. Fig. 7. For all mixed clusters small bin sizes were employed, $\Delta R < 0.03$ Å. These smaller bin sizes yield a more detailed picture of density profiles but tend to give larger statistical error, especially near the origin. However, despite both this and the relative inefficiency of binning for a single H_2 particle in an N -particle cluster, the statistical error in the H_2 density profiles is quite reasonable to within about 1 Å of the cluster center. Even for the largest cluster, H_2He_{19} , computed statistical error in each bin is 10% or less from 1 to 10 Å. (For He, the precision is of course much better; less than 5% from 0.5 to 12 Å for H_2He_{19} .) Once again, we point out that computational cost is not large, e.g., 27 Cray/X-MP14 minutes for the H_2He_{19} calculation.

Figures 6 and 7 demonstrate that H_2 is delocalized throughout the cluster, as is the case for He in both the pure and mixed clusters. This is not surprising considering the lighter mass of H_2 and the similarity of the H_2 -He and He-He potentials. Perhaps most interesting is that the greatest probability is not observed at the origin but peaks at some distance from the center. This point of maximum H_2 probability density increases from roughly 1 to 5 Å as the cluster increases from 5 to 20 particles, paralleling the increase in cluster size. Note that for H_2He_2 the probability density for H_2 simply mimics that of He [Fig. 6(a)] and that both the H_2 and the He density profiles are similar to that of He, (Fig. 4). This shows that H_2 can take the place of a He in any position, including the collinear arrangements which lead to the unique density profiles we have observed.

Table V summarizes a quantitative analysis of the H_2 probability peak. The second column measures the absolute position of the peak, R_{p_m} (relative to R_c) and clearly reflects the increase in size of the cluster as N increases. The third column measures the degree to which the peak in probability manifests itself: $\rho_m/\rho_0 = \rho_{\text{H}_2}(R_{p_m})/\rho_{\text{H}_2}(R=0)$ is the ratio of the maximum H_2 probability density to its value at the origin. (For H_2He_2 , the second maximum is used as ρ_m .) Given the statistical errors in ρ near the origin and the widths of the observed peaks, the quantities in Table V are

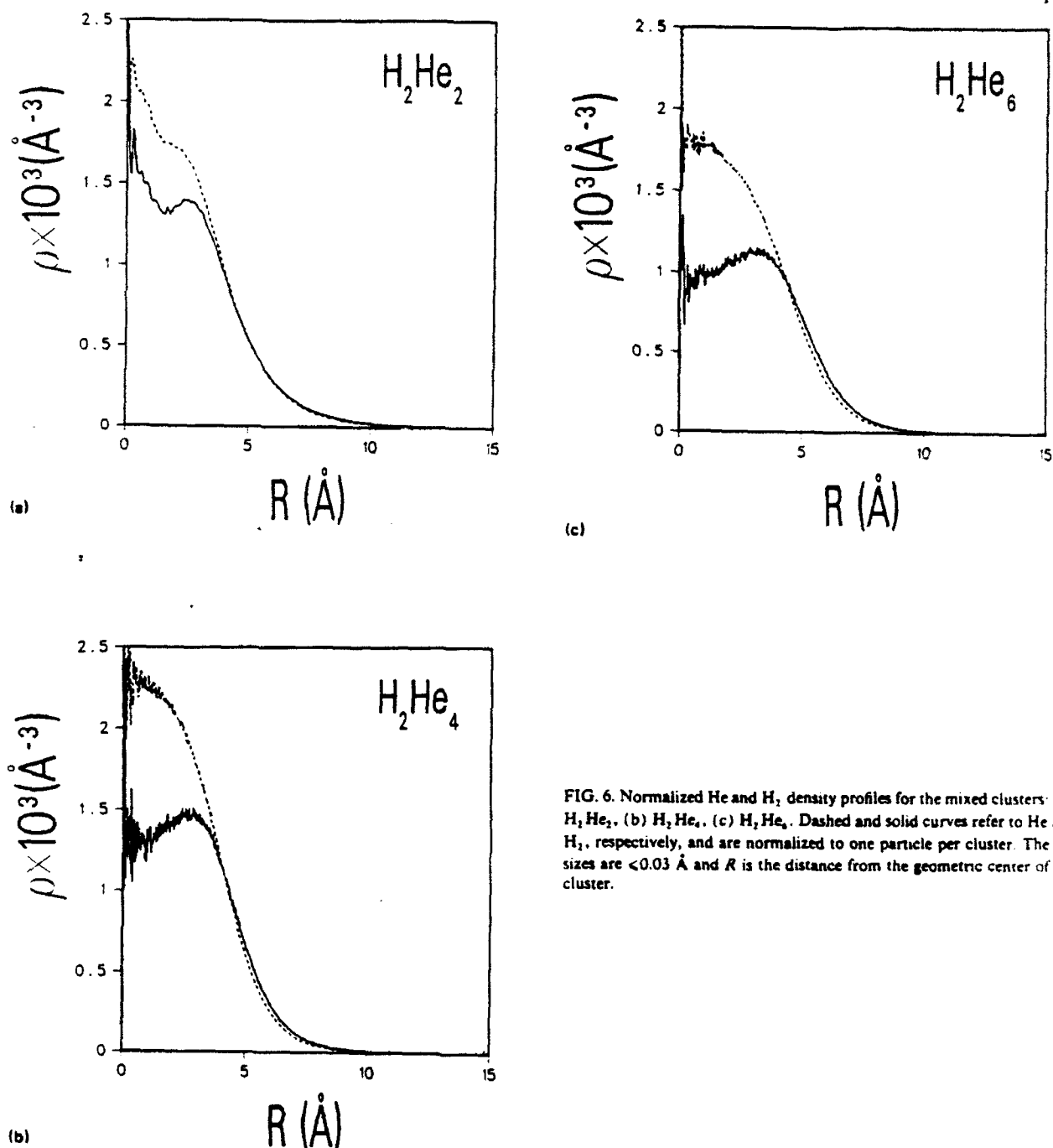


FIG. 6. Normalized He and H₂ density profiles for the mixed clusters: (a) H₂He₂, (b) H₂He₄, (c) H₂He₆. Dashed and solid curves refer to He and H₂, respectively, and are normalized to one particle per cluster. The bin sizes are <0.03 Å and *R* is the distance from the geometric center of the cluster.

estimated with some degree of uncertainty, i.e., 5%–10%. However, allowing for the qualitative nature of the results, it is obvious that the peak at R_{ρ_m} becomes more pronounced for the larger clusters, $N > 7$. Among the larger clusters, the H₂He₁₃ peak value of ρ_m/ρ_0 is significantly greater than the others, as is evident also from Fig. 7. The fourth column gives the ratio of the He density at R_{ρ_m} to its value at the origin, i.e., $\rho_{He}(R_{\rho_m})/\rho_{He}(R=0)$. The fifth column shows the amount of helium contained inside the peak position, i.e.,

$\int_0^{R_{\rho_m}} 4\pi \rho_{He}(R) R^2 dR$. Omitting the special H₂He₂ case, these last two columns of results show that the H₂ molecule tends to reside at greater distances from the cluster center for the larger clusters. However, the H₂ molecule shows no significant tendency to move further towards the cluster edge as the size increases from 13 to 19 He atoms; the peak becomes less pronounced (third column, Table V) and its position relative to the helium density only increases by a small amount (last two columns). In addition, the position of the

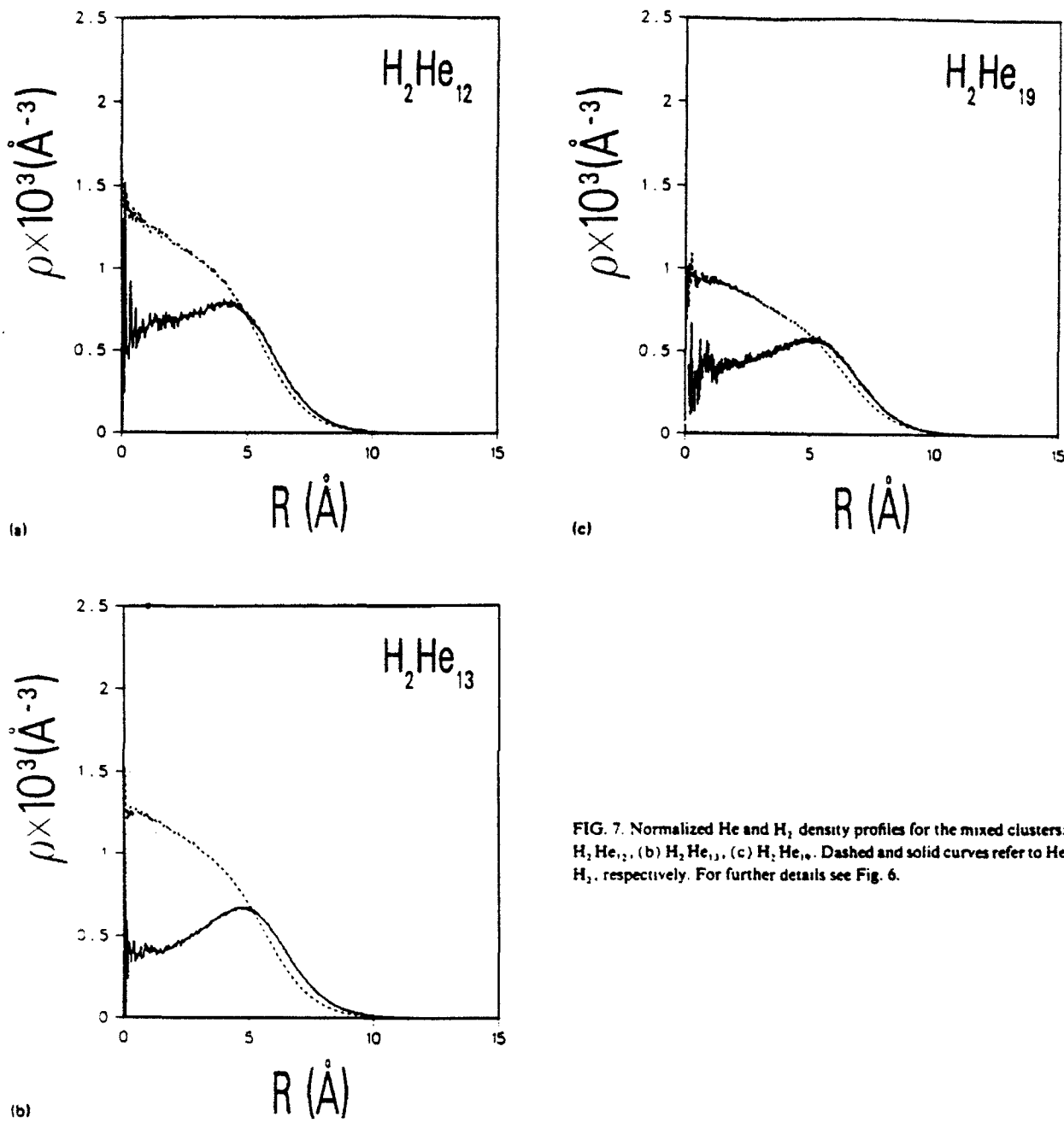


FIG. 7. Normalized He and H₂ density profiles for the mixed clusters: (a) H₂He₁₂, (b) H₂He₁₃, (c) H₂He₁₉. Dashed and solid curves refer to He and H₂, respectively. For further details see Fig. 6.

TABLE IV. Size comparisons between pure and mixed clusters.*

Cluster	$(\langle R^2 \rangle)^{1/2}$	Cluster	He		H ₂	
			$(\langle R^2 \rangle)^{1/2}$	P	$(\langle R^2 \rangle)^{1/2}$	P
He ₁	6.14	H ₂ He ₂	5.67	0.487	6.05	0.532
He ₂	5.44	H ₂ He ₃	5.48	0.487	5.88	0.526
He ₃	4.98	H ₂ He ₄	4.75	0.485	5.17	0.570
He ₄	5.11	H ₂ He ₅	5.02	0.490	5.37	0.579
He ₁₁	5.40	H ₂ He ₁₂	5.39	0.492	5.77	0.590
He ₁₃	5.45	H ₂ He ₁₃	5.48	0.494	6.12	0.657
He ₁₉	5.93	H ₂ He ₁₉	5.96	0.494	6.34	0.601

*The quantity $(\langle R^2 \rangle)^{1/2}$ is the rms distance from the cluster center, in \AA . P is the cumulative probability of finding the particle beyond the spherical shell in which half the particles are found on average (see text).

TABLE V. H_2 probability peak characteristics.*

Cluster	R_{p_m}	ρ_m/ρ_0 [H_2]	ρ_m/ρ_0 [He]	% He inside
H_2He_2	2.3	0.86	0.76	9.2
H_2He_4	1.3	1.05	0.89	2.1
H_2He_6	2.7	1.16	0.98	16.9
H_2He_8	2.9	1.28	0.83	16.7
H_2He_{12}	4.0	1.32	0.67	29.5
H_2He_{14}	4.4	1.68	0.65	35.8
H_2He_{16}	5.1	1.38	0.61	40.3

* R_{p_m} is the position of the H_2 maximum, in Å. ρ_m/ρ_0 is the ratio of the peak probability to the central ($R = 0$) probability, for H_2 and He, respectively. The % He inside is measured with respect to R_{p_m} .

peak lies well inside the cluster surface, i.e., at least 60% of the integrated He density lies beyond the H_2 peak. Therefore, the H_2 density profiles show some localization, most noticeable for the larger clusters (> 12 He atoms), and indicate absorption between the cluster center and its exterior. This perhaps reflects the fact that H_2 has been found to penetrate bulk liquid helium.⁸

Figures 8 and 9 show the particle separation probability density functions $p(r)$ for the He-He (dashed lines) and H_2 -He separations (solid lines). These show the same general trends with size which are apparent in Figs. 4 and 5. Differentiation between H_2 and He is not large. However, the H_2 -He distributions are consistently smaller at small separations and consistently more diffuse at large separa-

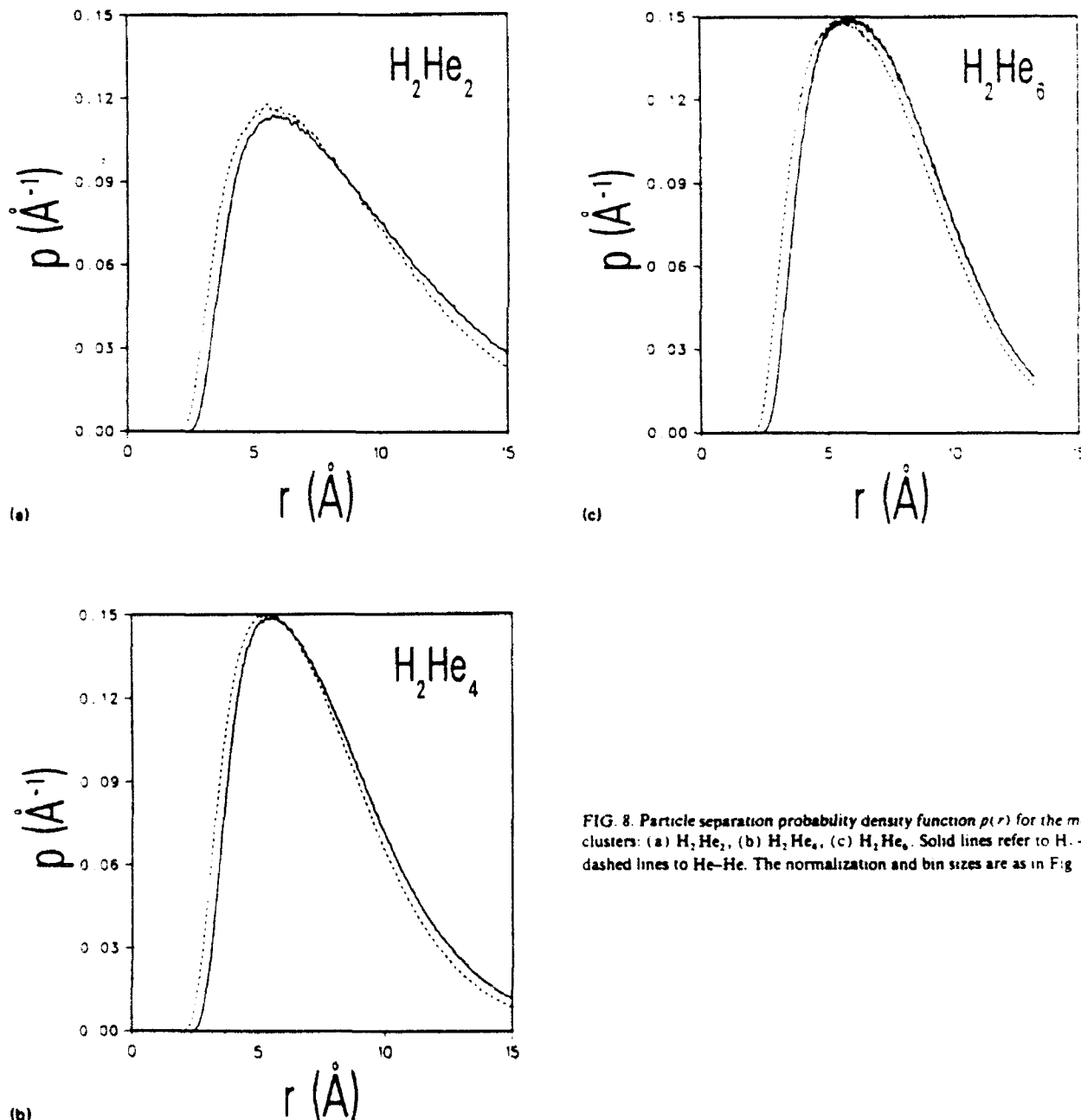


FIG. 8. Particle separation probability density function $p(r)$ for the mixed clusters: (a) H_2He_2 , (b) H_2He_4 , (c) H_2He_6 . Solid lines refer to H_2 -He, dashed lines to He-He. The normalization and bin sizes are as in Fig. 4.

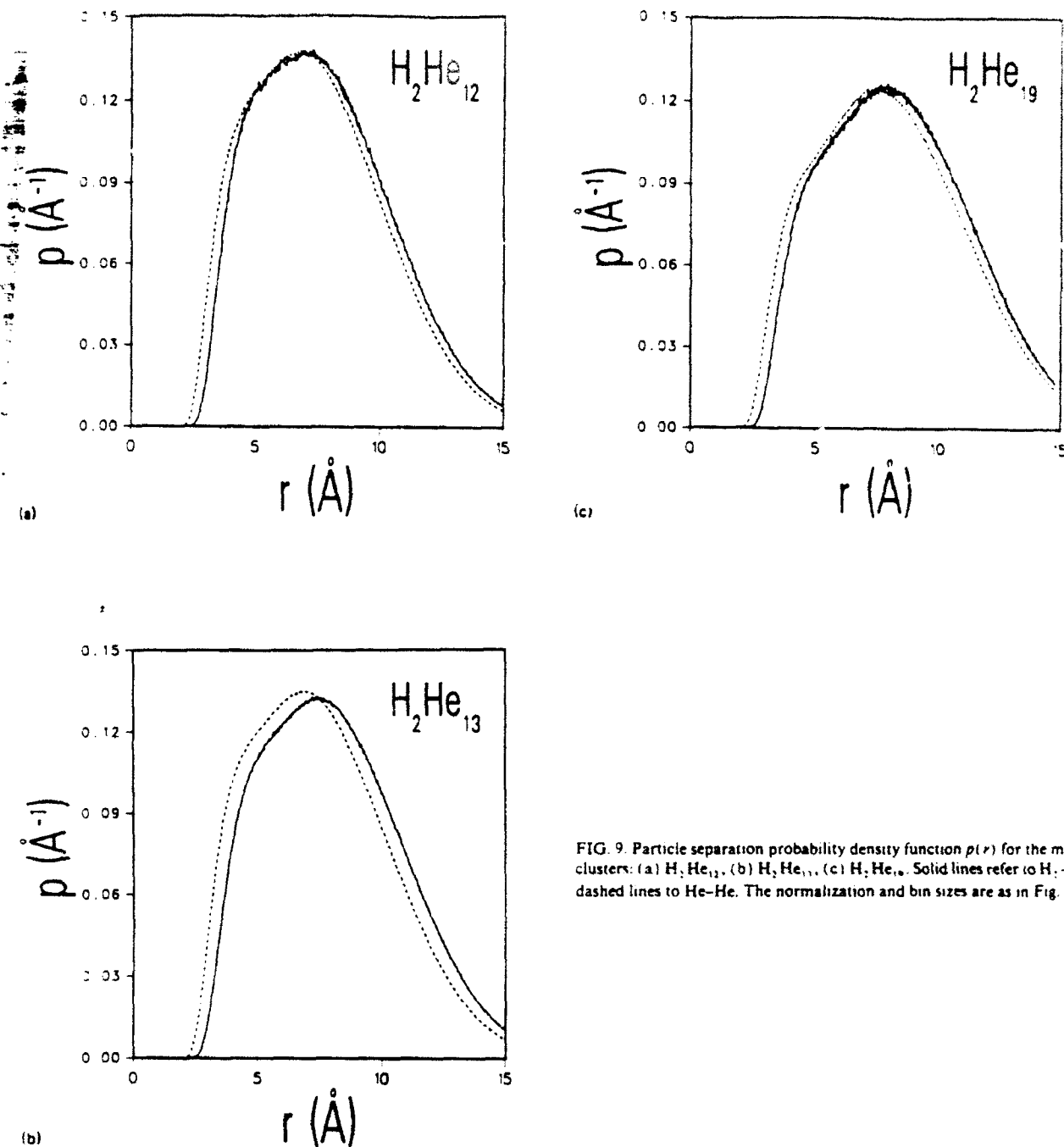


FIG. 9. Particle separation probability density function $p(r)$ for the mixed clusters: (a) H_2He_{12} , (b) H_2He_{13} , (c) H_2He_{19} . Solid lines refer to $\text{H}_2\text{-He}$, dashed lines to He-He . The normalization and bin sizes are as in Fig. 4.

tions than the He-He distributions. The trend at small r is easily understood from the interaction potentials, cf. Fig. 1, where the $\text{H}_2\text{-He}$ potential becomes highly repulsive sooner than that of He-He. The behavior at large r is less transparent. The $\text{H}_2\text{-He}$ potential has a greater well depth and is more attractive at larger separations. On the other hand, the lighter mass of H_2 tends to reduce $\text{H}_2\text{-He}$ binding vs He-He binding. This factor, as well as the fact that helium atoms can get closer to themselves than to H_2 , may also explain why

the maximum probability of finding H_2 is somewhat removed from the cluster center.

As is the case for the density profiles, the particle separation distributions p stand out for $\text{H}_2\text{-He}$ vs He-He, clearly visible in Fig. 9, is most pronounced for H_2He_{13} amongst the larger clusters. The implication here, as with the density profiles, is that He_{13} possesses a somewhat enhanced degree of stability with respect to H_2 penetration.

TABLE VI. Wave-function parameters for He_N (in atomic units).

N	3	4	5	7	13	14	20
$a/10$	-0.10229	-0.10229	-0.18365	-0.10700	-1.0595	-1.0706	-0.60074
b	-1.34028	-1.34028	-1.30676	-1.41058	-0.97588	-1.04666	-1.04664
α	1.18370	1.18378	1.03509	0.52691	0.60314	0.54500	0.54503
a_0	0.14630	0.14630	0.14630	-0.97190	-1.43987	-1.32361	-1.30801
a_1	-20.046	-23.447	-23.034	-23.037	-29.9399	-30.1935	-38.8646
a_2	151.69	159.923	158.499	158.50	200.994	199.831	310.061
a_3	-746.490	-742.004	-782.170	-782.170	-851.450	-845.506	-1.370.01
a_4	1709.00	1710.60	1842.10	1842.10	1809.01	1808.98	2484.45
a_5	-4404.1	-4403.6	-4344.3	-4344.3	-4352.3	-4354.1	-3674.6

IV. CONCLUSIONS

This first quantum-mechanical study of an impurity species in a rare-gas cluster shows the lower-mass H_2 impurity to be extensively delocalized in finite helium clusters. Considering the similar mass and interaction potential with He (cf. Fig. 1), this is consistent with observations of ^3He delocalization in bulk helium (^4He).²⁶ However, much less is known about H_2 or any other molecular impurity in bulk helium. It will be useful to follow this trend for cluster sizes larger than those studied here, to ascertain whether the H_2 species is surface attached, or embedded in the interior, as appears to be the case thus far, as we approach bulk systems. In addition, possible localization of the H_2 and of other impurities at larger cluster sizes is of interest. Finally, incorporating the weak anisotropy of the H_2 - He potential is worth considering.

The wave-function forms employed here for both the mixed clusters H_2 - He_N and the pure He_N reference systems present a radical departure from previous analytic forms used in variational Monte Carlo ground-state studies. No

one-particle term is employed, and the two-particle term is explicitly constructed by fitting to the bound numerical solution of H_2He , which allows much greater sensitivity to the long-range part of the potential than in previous forms. Accurate representation of the diffuse tail of the two-body factors appears to be extremely important in obtaining accurate energies. We note here that for He_N and He_N , the energies lie below the previously computed exact GFMC values. In Ref. 11, we find that this results from the use by GFMC of the 1979 potential which is slightly shallower than the most recent one (1987) employed here. The high level of accuracy obtained here at the VMC level with just the two-particle term, even for $N = 20$, also suggests that addition of the three-particle terms known to be important for the larger clusters may well provide a new level of accuracy at the VMC level for these larger systems as well. It will be very interesting to see how well the lack of one-particle term does at larger N . This term has been required in previous studies by us and others because of the modified liquid-state asymptotic form imposed on the two-particle term. Note that the new form employed here does have the flexibility to revert to

TABLE VII. Wave-function parameters for H_2He_N (in atomic units).

N	He-He parameters for H_2He_N						
	2	3	4	6	12	13	19
$a/10$	-0.57743	-0.083449	-0.39186	-0.46782	-1.0595	-1.0241	-0.84034
b	-1.07843	-1.33566	-1.59036	-1.37276	-1.01685	-1.02328	-0.97641
α	0.970574	1.171530	0.791906	0.645789	0.603138	0.604093	0.553315
a_0	-1.30832	0.11479	0.63834	-0.75800	-1.50801	-1.40582	-1.38608
a_1	-23.932	-20.046	-25.642	-24.427	-30.753	-33.700	-38.875
a_2	165.288	151.690	157.665	158.838	202.829	226.526	310.059
a_3	-734.485	-746.490	-782.390	-782.049	-852.536	-907.670	-1307.01
a_4	1715.65	1709.00	1842.20	1842.13	1813.57	1792.85	2484.45
a_5	-4401.3	-4404.1	-4050.3	-4040.3	-4348.4	-4350.0	-3674.6

N	H ₂ -He parameters for H_2He_N						
	2	3	4	6	12	13	19
$a/100$	-0.65703	-0.050860	-0.050865	-0.36243	-0.36243	-0.41131	-0.28601
b	-0.62584	-1.43377	-1.41175	-1.12054	-0.73013	-0.71535	-0.68577
α	1.400470	1.147770	1.135880	1.151390	1.151390	1.153680	1.069830
a_0	-2.13962	-0.65703	-0.16498	-0.87913	-0.92728	-0.82508	-0.90315
a_1	-6.163	-14.043	-15.359	-14.923	-12.744	-14.607	-14.612
a_2	112.344	121.898	121.843	123.210	122.727	131.758	131.757
a_3	-719.100	-710.496	-710.504	-710.000	-711.061	-730.737	-730.737
a_4	1723.29	1726.98	1726.97	1727.10	1726.35	1715.99	1715.99
a_5	-7455.6	-7454.4	-7454.2	-7454.4	-7454.7	-7458.0	-7458.0

Variational and diffusion Monte Carlo techniques for quantum clusters

R. N. Barnett and K. B. Whaley

Department of Chemistry, University of California, Berkeley, California 94720

(Received 21 August 1991; revised manuscript received 18 November 1992)

The $H_2\cdot^4He$ dimer and small 4He clusters are studied using Monte Carlo sampling techniques. We consider alternative wave-function forms in order to obtain high accuracy efficiently. For the smaller systems, both guided and unguided Metropolis walks are used and the efficiencies are studied. Of particular concern is accurate sampling at small particle separations and the behavior of the local energy in this regime. As a final step, we compute exact energies by a diffusion Monte Carlo method. We obtain converged energies significantly below the Green's-function Monte Carlo values, which employed an earlier He-He potential with a slightly shallower well. For He_2 and He_3 , the Green's-function Monte Carlo energies are reproduced when employing the same potential. However, for the 112-atom cluster, our converged energy lies below the Green's-function Monte Carlo value. Second-order estimates of the exact density profiles and particle separation distributions, p , are also determined. For the 14- and 20-atom clusters, second-order estimates of p show enhanced structure in comparison to variational Monte Carlo results. Statistically meaningful oscillations in the second-order estimates of the exact density profiles are not observed.

PACS number(s): 36.40.+d, 67.40.Db, 02.70.-c, 03.65.Ge

I. INTRODUCTION

Atomic and molecular clusters have become of interest to both theorists and experimentalists [1]. Of particular concern are structure, phase transitions, binding energies, and excitation spectra, and the behavior of these properties as the bulk is approached.

We are interested in studying atomic and molecular clusters, both pure and with impurities attached, using Monte Carlo techniques. Such approaches thus far possess the greatest possibility of yielding high accuracy for theoretical methods. To enhance the capabilities of Monte Carlo for these systems, we consider alternative wave-function forms and the efficient optimization of wave-function parameters in studying weakly bound quantum clusters. To start with, we study the H_2He complex (from here on 4He is assumed). This system is quite useful as it provides a very weakly bound, highly repulsive potential, test case for the initial wave-function form we employ.

As a further development, we employ diffusion Monte Carlo (DMC). We use this approach to compute exact ground-state energies for helium clusters with the most up-to-date potential. In addition to increased accuracy in the energy and structural features such as the density profile, the DMC approach serves to provide benchmarks for evaluating wave-function quality. This is pertinent for the helium clusters for which exact energies resulting from the most recent pair potential have not yet been computed.

The remainder of the paper is organized as follows. In Sec. II we discuss Monte Carlo integration techniques, and in Sec. III the exact diffusion Monte Carlo approach. The wave-function forms and optimization technique we employ are presented in Sec. IV. In Sec. V we present results for a range of small clusters ($N \leq 20$ and $N = 112$).

Section VI presents conclusions concerning the wave-function accuracy and sampling efficiency for all techniques.

II. MONTE CARLO INTEGRATION TECHNIQUES

Multidimensional integration is performed by Monte Carlo in order to obtain wave-function expectation values. This is achieved by sampling points, $\mathbf{R} = (r_1, r_2, \dots, r_N)$, from a probability density function $p(\mathbf{R})$. Expectation values of coordinate operators $A(\mathbf{R})$ are then computed as

$$\bar{A}_M \equiv M^{-1} \sum_{i=1}^M A(\mathbf{R}_i), \quad (1)$$

with $\{\mathbf{R}_i\}$ sampled from p . As M becomes large, \bar{A}_M approaches the average of $A(\mathbf{R})$ over $p(\mathbf{R})$.

We employ two variants of the Metropolis walk [2,3] to sample p . The first of these is the widely used and very simple "unguided" walk. For a point at \mathbf{R} , a new point is sampled from a transition probability density $T(\mathbf{R} \rightarrow \mathbf{R}')$ which is simply constant within a cube and zero outside. Thus moves are generated by

$$\mathbf{R}' = \mathbf{R} + \Delta(\xi - 0.5), \quad (2)$$

where ξ is a vector whose components are uniform random variates between 0 and 1.

This "unguided" walk attempts to move uniformly through coordinate space without regard to the form of $|\Psi|^2$. Therefore a more efficient scheme of choosing attempted moves is likely. This is the basis of a guided or "smart" Metropolis walk, which is also known as importance sampling. We now choose the transition density to be

$$T(\mathbf{R} \rightarrow \mathbf{R}') = (4\pi\Delta)^{-3N/2} \exp\{-[\mathbf{R}' - \mathbf{R} - \Delta\mathbf{F}(\mathbf{R})]^2/4\Delta\}. \quad (3)$$

Sampling from this transition density requires that

$$\mathbf{R}' = \mathbf{R} + \Delta\mathbf{F}(\mathbf{R}) + \sqrt{2\Delta} \mathbf{x}. \quad (4)$$

The components of \mathbf{x} are Gaussian random numbers with a mean of zero and a variance of unity, which we obtain by the Box-Mueller algorithm [4]. The "guiding force," $\mathbf{F} = \nabla|\Psi|^2$, acts to push moves in the direction of most rapidly increasing $|\Psi|^2$.

The major consideration for the approaches discussed here is the value of Δ which yields the most efficient sampling. The optimum choice lies between a small value, which yields a high acceptance rate but a large degree of correlation between moves, and a large value, which gives large attempted displacements but a very small acceptance rate so that correlation is large. The optimum Δ is often taken to be that which yields an average acceptance rate (or ratio) of roughly 0.5. Here we consider a further quantitative measurement of the efficiency with which configuration space is sampled, namely, the average displacement of moves during the walk, $\langle \Delta\mathbf{R} \rangle$. (A rejected move contributes a value of zero to this average.)

III. DIFFUSION MONTE CARLO

Although the Metropolis algorithm provides a means for computing expectation values of a given wave function, accuracy is limited by the quality of Ψ . However, exact Monte Carlo approaches are well known. These approaches are often generically referred to as quantum Monte Carlo and fall into two categories, Green's-function Monte Carlo (GFMC) and diffusion Monte Carlo. The former has been applied to a wide range of problems and derives from consideration of the time-independent Schrödinger equation. Initial work was on the helium atom [5] and liquid helium [6,7], and later applications include electronic structure calculations [8,9] and computations on helium clusters [10–12].

DMC starts with the time-dependent Schrödinger equation in imaginary time and has been employed mostly in electronic structure calculations [13–17]. Recent work has also included helium clusters and other van der Waals species [18–20]. The DMC approach we employ is very similar to that of Reynolds *et al.* [15] and is outlined below.

Writing the Schrödinger equation in imaginary time, $t \rightarrow t/i$, and setting $\hbar = 1$ we have

$$-\frac{\partial\Phi(\mathbf{R},t)}{\partial t} = (H - E_R)\Phi(\mathbf{R},t). \quad (5)$$

The reference energy E_R only affects the (imaginary) time dependence of $\Phi(\mathbf{R},t)$. It is easily shown that at large t the ground state dominates, leaving

$$\Phi = \exp[-t(E_0 - E_R)]\phi_0. \quad (6)$$

Note that the choice of $E_R \approx E_0$ is useful in removing the time dependence from the asymptotic solution.

Importance sampling is implemented by choosing a

probability density function $f \equiv \Psi\Phi$, where Ψ is a trial wave function. Rewriting Eq. (5) in terms of f gives

$$-\frac{\partial f}{\partial t} = -D\nabla^2 f + D\nabla \cdot [f\mathbf{F}(\mathbf{R})] + [E_L(\mathbf{R}) - E_R]f, \quad (7)$$

where

$$H = -D\nabla^2 + V, \quad D\nabla^2 \equiv \sum_i (2m_i)^{-1}\nabla_i^2,$$

$E_L \equiv \Psi^{-1}H\Psi$ is the local energy, and once again $\mathbf{F} \equiv \nabla \ln|\Psi|^2$. Note that terms on the right-hand side of Eq. (7) correspond to diffusion, drift, and branching, respectively. The asymptotic form of f follows from Eq. (6) and is

$$f(\mathbf{R},t) = \exp[-t(E_0 - E_R)]\Psi(\mathbf{R})\phi_0(\mathbf{R}). \quad (8)$$

When f takes this form, expectation values over f are independent of t , i.e.,

$$\langle A \rangle_f \equiv \int f(\mathbf{R},t)A(\mathbf{R})d\mathbf{R} / \int f(\mathbf{R},t)d\mathbf{R} = \int \Psi(\mathbf{R})\phi_0(\mathbf{R})A(\mathbf{R})d\mathbf{R} / \int \Psi(\mathbf{R})\phi_0(\mathbf{R})d\mathbf{R}.$$

For $A(\mathbf{R}) = E_L(\mathbf{R})$, it is easily shown that $\langle E_L \rangle_f = E_0$, so that the ground-state energy is obtained as the average of E_L over f . The time development of f is given by

$$f(\mathbf{R}',t+\tau) = \int d\mathbf{R} f(\mathbf{R},t)G(\mathbf{R} \rightarrow \mathbf{R}',\tau), \quad (9)$$

where the Green's function G describes a move from \mathbf{R} to \mathbf{R}' in time τ . The Green's function is a solution of Eq. (7) with the boundary condition $G(\mathbf{R} \rightarrow \mathbf{R}',0) = \delta(\mathbf{R} - \mathbf{R}')$. For all but a few simple Hamiltonians, the Green's function is unknown. Here, we employ an analytic "short-time" approximation to G which takes the form

$$G_a(\mathbf{R} \rightarrow \mathbf{R}',\tau) = (4\pi D\tau)^{-3N/2} \times \exp\{-[\mathbf{R}' - \mathbf{R} - D\tau\mathbf{F}(\mathbf{R})]^2/4D\tau\} \times \exp\{-\tau\{[E_L(\mathbf{R}') + E_L(\mathbf{R})]/2 - E_R\}\}. \quad (10)$$

The approximate nature of G_a is clear from Eq. (10): during the course of a move from \mathbf{R} to \mathbf{R}' in time τ , the drift [determined by $\mathbf{F}(\mathbf{R})$] and branching (dependent on E_L) are assumed to be constant. While error in G_a vanishes as $\tau \rightarrow 0$ [21–23], for the practical case, i.e., $\tau \neq 0$, the asymptotic f only approximates $\Psi\phi_0$, and computed results will differ from the corresponding averages over $\Psi\phi_0$. This difference, referred to as time-step bias, may either be removed by extrapolation or made insignificant by using values of τ such that the bias is less than the statistical error.

To reduce time-step bias, an acceptance-or-rejection step is employed [15]. That is, moves are accepted with a probability A given by

$$A(\mathbf{R} \rightarrow \mathbf{R}',\tau) = \min\{1, w(\mathbf{R} \rightarrow \mathbf{R}',\tau)\}, \quad (11)$$

and

$$w(\mathbf{R} \rightarrow \mathbf{R}',\tau) = \frac{|\Psi(\mathbf{R}')^2|G_a(\mathbf{R}' \rightarrow \mathbf{R},\tau)}{|\Psi(\mathbf{R})|^2G_a(\mathbf{R} \rightarrow \mathbf{R}',\tau)}. \quad (12)$$

Including the factor A plays an important role. As Ψ approaches the exact solution ϕ_0 , the branching becomes constant and G_s is essentially the transition density given in Eq. (3) with $\Delta = D\tau$. In this instance, DMC reduces to a guided Metropolis walk and $f(=|\phi_0|^2)$ is sampled without time-step bias—for any value of τ . Use of A has been found to greatly reduce time-step bias [24] because the acceptance-or-rejection step eliminates time-step bias to the extent that Ψ resembles ϕ_0 .

We conclude this section with a discussion of several technical details. In the DMC [and Metropolis-walk or variational Monte Carlo (VMC) computations, ten independent ensembles of 100 walkers are propagated in parallel yielding ten independent estimates, of, for example, the energy, from which the average and its statistical error are obtained. If greater precision is desired, more runs are performed in this manner. This structure is useful in that for each set of runs an estimate of statistical error unbiased by serial correlation is computed.

Updating the reference energy E_R is useful for minimizing the time dependence of the ensemble. For a given number [or population, $P(0)$] of points sampled from $f(0) = \Psi\phi_0$ at the beginning of the DMC walk, we have

$$P(0) = \int f(\mathbf{R}, 0) d\mathbf{R}. \quad (13)$$

From the asymptotic form of f it is easily seen that

$$P(t) = \exp[-t(E_0 - E_R)] P(0). \quad (14)$$

Note that Eq. (14) indicates that an estimate of E_0 may be obtained from the change in the ensemble size over time. This estimate, usually referred to as the growth energy (E_G), often possesses a different dependence on the time step than does the average of the local energy E_L . Therefore, to reduce the long-term growth or decay of ensemble size, at each time step we perform a short run to estimate E_G and then set E_R equal to this estimate when computing the reported results.

Another point concerns the renormalization of the ensemble population P . Even when E_R is equal to the growth estimate of E_0 , fluctuations in P arise from fluctuations in E_G , which are in turn caused by variations in the local energy, as the ensemble is propagated. If the statistical error in E_G over the ensemble is σ_{E_G} , then from Eq. (14) the relative statistical error in P is seen to increase proportionally to time as

$$\sigma_P/P = t\sigma_{E_G}. \quad (15)$$

Therefore, in keeping the ensemble size reasonable, it is useful to renormalize the population [back to P_0 ($= 100$)] at intervals during the walk. However, as noted previously [25], renormalization introduces an error which decreases as the frequency of renormalization decreases. (Generally, this error is not noticeable unless the propagation time between renormalizations is very short.) Here, we divide each run into blocks, and at the end of each block the population is renormalized to 100 walkers. We vary block propagation times (10^4 – 10^6 hartree^{–1}) to verify that "renormalization" bias is negligible.

The final point concerns the implementation of branch-

ing. As seen from Eq. (10), the branching factor for a move from \mathbf{R} to \mathbf{R}' is

$$b(\mathbf{R}, \mathbf{R}') = \exp(-\tau\{[E_L(\mathbf{R}') + E_L(\mathbf{R})]/2 - E_R\}). \quad (16)$$

Branching may be implemented by obtaining an integer $M = \text{int}[b(\mathbf{R}, \mathbf{R}') + \xi]$, where $\text{int}(x)$ is the largest integer that is $\leq x$ and where ξ is a uniform random variate uniformly distributed between 0 and 1 so that $M = b$ on average, and creating M copies of walkers at \mathbf{R}' . Alternatively, one may assign a weight $w(\mathbf{R}') = b(\mathbf{R}, \mathbf{R}')w(\mathbf{R})$ to the walker at \mathbf{R}' . Since M equals b only on average, assigning (or carrying) weights would seem preferable. However, carried weights diverge towards 0 or ∞ as the walk proceeds, giving rise to the possibility that an ensemble may be effectively composed of a few walkers with very large relative weights. In this event, the sampling is inefficient as only a few of the many walkers being propagated contribute to the computed averages. Therefore we employ a combination of carrying weights and copying. Weights are carried unless $w \leq w_{\min}$ or $w \geq w_{\max}$. If either of the bounds are exceeded then $M_w = \text{int}(w + \xi)$ copies are made, and for $w \geq w_{\max}$ each copy is assigned a weight of w/M_w . For the DMC results reported here, $w_{\min} = 0.1$ – 0.4 and $w_{\max} = 2$.

IV. TRIAL FUNCTION FORM AND OPTIMIZATION

A. Trial functions

We seek ground-state wave functions for bosonic systems. Such wave functions are nodeless and therefore may be taken as everywhere positive. A convenient representation takes the form

$$\Psi(\mathbf{R}) = \exp \left[\sum_I T_I(\mathbf{R}) \right], \quad (17)$$

where in the completely general case

$$T_I(\mathbf{R}) = \sum_{\substack{i,j,k,\dots \\ (i < j < k < \dots)}} t_I(r_i, r_j, r_k, \dots). \quad (18)$$

In practice I is taken to be ≤ 3 so that the wave function is reasonably compact. Since the potential is given by the sum of pairwise interactions, we omit T_1 and instead start with two-body terms. (One-body terms have been employed in previous studies of clusters [10,26,27], but are not necessary.) We then add on three-body terms for increased accuracy if desired. This reflects the fact that two-body effects should be most important, especially for weakly bound clusters, followed by three-body effects, etc.

As is common practice, we employ a two-body term which is a function only of particle separations, i.e.,

$$T_2(\mathbf{R}) = \sum_{\substack{i,j \\ (i < j)}} t_2(r_i, r_j) = \sum_{\substack{i,j \\ (i < j)}} t_2(r_{ij}). \quad (19)$$

This term is both translationally and rotationally invariant, i.e., $P_{c.m.} T_2 = 0$ and $L T_2 = 0$, as required for the ground-state wave function. Given the importance of two-body effects, it is useful to explore optimal forms for

t_2 . In this vein, H_2He , the first "cluster" in the H_2He_N series, provides an excellent test case as a weakly bound species with an interaction potential very similar to that of He-He. Therefore a form of t_2 which accurately describes H_2He may prove advantageous for the helium clusters as well.

The initial form of t_2 is motivated by our studies of H_2He . For the interaction potential, we use a Lennard-Jones plus van der Waals fit [28] to the *ab initio* data of V_0 computed by Meyer, Hariharan, and Kutzelnigg [29]. Since our potential is a function only of the He distance from the H_2 center of mass, the Schrödinger equation for this system can now be reduced to a one-dimensional problem. A numerical solution for the ground state, $\phi_0^{(N)}$, is obtained with the finite difference algorithm of Schatz [30]. The next step consists of considering forms for Ψ and fitting them to $\phi_0^{(N)}$. The accuracy of both the wavefunction fit and the computed energy expectation value allow an assessment of the quality of Ψ .

In determining a useful analytic form for Ψ , we treat the long- and short-range behaviors separately. That is, Ψ takes the form

$$\Psi(r) = \Psi_s(r)\Psi_l(r), \quad (20)$$

where s and l denote the short- and long-range functions,

respectively. The short-range form is chosen to be constant at large r . Given the form of V at small r , a natural choice for Ψ_s is

$$\begin{aligned} \Psi_s(r) &= \exp[P(u)], \quad u = r^{-1}, \\ P(u) &= \sum_{k=0}^5 a_k u^k. \end{aligned} \quad (21)$$

The bound on the powers included in P results from the desire to limit singularities in the kinetic energy to be no greater than r^{-12} , given that this is the dominant singularity in our potential [28]. A high-quality form of Ψ_s was found to be

$$\Psi_s = r^b \exp[ar^a]. \quad (22)$$

Since Ψ_s is very nearly constant at large r , we first fit Ψ_s to $\ln[\phi_0^{(N)}]$ in this domain to determine a , b , and a . We then determine the short-range parameters $\{a_k\}$ by fitting in the highly repulsive and in the well regions. The range of points included in the short- and long-range fits determines the parameters, which are listed in Table I. We find that the analytic wave function Ψ is nearly indiscernible from the numerical solution $\phi_0^{(N)}$, and the energy is reproduced to high accuracy, -0.02443 versus -0.02461 K—an error of only 0.7%.

TABLE I. Wave-function parameters.

Parameter \ Cluster	H_2He	He_{14}	He_{20}	$He_{112}(T_2)$	$He_{112}(T_2 + T_3)$
a	-0.00731522	-0.107061	-0.062	-0.01000	-0.01400
b	-1.438143	-1.04666	-1.055	-0.85000	-0.85500
a	1.13839	0.559995	0.545	0.545031	0.545031
a_0	0.1536	-1.32361	-1.30801	-1.30801	-1.30801
a_1	-14.04255	-30.1935	-38.8646	-38.8646	-38.8646
a_2	121.49628	199.831	310.061	310.061	310.061
a_3	-710.89788	-845.506	-1370.01	-1370.01	-1370.01
a_4	1726.9756	1808.98	2484.45	2484.45	2484.45
a_5	-7454.4214	-4354.11	-3674.60	-3674.60	-3674.60
λ_0		0.012	0.012		0.009
ω_0		1.60	1.60		1.8
r_0		5.0	5.0		4.5
λ_1		0.043	0.043		0.031
ω_1		2.025	2.025		2.225
r_1		3.225	3.225		3.225
Parameter \ Cluster	He_3	He_7	He_{20}		
a_0	-3.2319500	-3.24739	-3.41398		
a_1	-0.0684583	-0.0469850	-0.0191689		
a_2	8.55	8.65	9.20		
a_3	0.8400750	0.914958	0.873622		
β_0	0.0861481	0.0695676	0.0691040		
t_0	-682.979	-682.409	-675.000		
t_1	588.918	590.085	590.085		
t_2	-205.068	-203.773	-203.775		
t_3	34.1321	33.1709	33.1633		
t_4	-2.62822	-2.46631	-2.48577		
t_5	0.0601202	0.0533509	0.0588524		

The H_2 -He wave function gives a two-body function,

$$t_2(r) = b \ln r + ar^\alpha + \sum_{k=0}^5 a_k r^k, \quad (23)$$

which we have employed in VMC computations of helium clusters with and without a H_2 impurity [28]. The form of t_2 is structurally similar to forms used previously [10,26,27]. The differences are that in the short-range form all powers of r^{-1} up to five are included here, and there is an added flexibility in the long-range form, introduced by the exponent α . As discussed above, the short-range component of t_2 is based on our H_2 -He potential which takes a Lennard-Jones form at small separations [28]. While the shape of this potential is similar to that of He-He [31], the analytic forms are quite different. Therefore it is of interest to consider entirely new forms for t_2 based on the short-range behavior of the He-He potential. We employ here the most recent HFD-B(HE) potential of Aziz, McCourt, and Wong [31] for all calculations unless it is explicitly stated that the earlier HFDHE2 [32] potential is used.

We give special emphasis to regions of small separation because the local energy generally possesses its greatest fluctuations as r becomes small. Therefore a two-body form which is more physically correct in this domain will reduce fluctuations in E_L , yielding greater precision, and hopefully greater accuracy, in computed energies. Our new t_2 takes the form

$$t_2'(r) = T(r)v(r) + a_0 + a_1 r + \gamma \ln r, \quad (24)$$

where

$$v(r) = a_v \exp(-\alpha_v r - \beta_v r^2) \quad (25)$$

mimics the short-range form of the He-He potential [31], and

$$T(r) = \sum_{k=0}^{n_k} t_k r^k, \quad (26)$$

with $n_k = 5$. We have chosen $\gamma = 0$ leaving only a singularity of r^{-1} in E_L , arising from the kinetic energy. Other permissible values are $\gamma < \frac{1}{2}$ which give an r^{-2} singularity but a finite statistical error in E_L . With $\gamma = 0$, $t_0 a_v$ negative and large gives a wave function which is very small but remains nonzero at $r = 0$. This reflects the fact that the potential converges to a very large but finite value at $r = 0$.

Overall, in comparison to Eq. (23), t_2' gives added emphasis to domains containing small particle separations and somewhat less emphasis to large r . It is hoped that, by directly including a "potential-like" function in Ψ , the highly repulsive potential term will be better canceled by the kinetic contribution, producing smaller fluctuations in E_L at small values of r .

The use of a three-body term in ground-state wave functions has yielded significant improvements in descriptions of both the liquid [33-37] and clusters [10]. Here, we employ the description of three-body correlations used previously in microscopic studies of quantum clusters [10,26,27,38], namely,

$$T_3(\mathbf{R}) = \lambda_0 \sum_i \left[\Gamma_0^2(i) - \sum_{j \neq i} \xi_0^2(r_{ij}) \right] + \lambda_1 \sum_i \left[|\Gamma_1(i)|^2 - \sum_{j \neq i} \xi_1^2(r_{ij}) r_{ij}^2 \right], \quad (27)$$

with

$$\Gamma_i(i) = \sum_{j \neq i} \xi_i(r_{ij}) r_{ij}^i, \quad i = 0, 1. \quad (28)$$

In Eqs. (27) and (28), we have

$$\xi_0(r) = (r - r_0) \exp \left[- \left(\frac{r - r_0}{w_0} \right)^2 \right], \quad (29)$$

$$\xi_1(r) = \exp \left[- \left(\frac{r - r_1}{w_1} \right)^2 \right].$$

Derivatives of T_3 are evaluated analytically. This is actually faster than finite difference because derivatives by finite difference require three evaluations of the exponentials in Eqs. (29) while analytic computation requires only one. Overall, adding T_3 to T_2 only increased computation time by about 85% for the 14-, 20-, and 112-atom clusters.

B. Optimization

Wave-function parameters are optimized by hand and by conjugate-gradient line minimization. Although crude, varying parameters by hand is quite useful in complementing more sophisticated techniques. Since initial wave-function parameters are often quite poor, hand optimization can quickly yield large improvements. The resulting wave function can then be used as input for the more sophisticated optimization techniques.

The conjugate-gradient technique [39] seeks a local minimum by moving in directions in parameter space which are conjugate to each other, leading to efficient convergence. Essentially, the algorithm consists of successive line minimizations in parameter space. This procedure requires the computation of the quantity being minimized and of its first derivatives with respect to the wave-function parameters. Here, we consider

$$s^2 = \frac{\langle \Psi | [E_L - E_g]^2 | \Psi \rangle}{\langle \Psi | \Psi \rangle}. \quad (30)$$

This quantity is useful in that one may seek either a minimum in the energy by choosing $E_g \ll \langle E_L \rangle$ or in the variance by choosing $E_g = \langle E_L \rangle$. In the first case, minimizing the energy yields global accuracy, and, in the second, minimizing fluctuations in the local energy emphasizes local accuracy in Ψ . Since computed energies are most often compared in discussions of accuracy, we focus on minimizing the energy.

The integrations in Eq. (30) are performed by averaging over a fixed set of points sampled from a distribution $|\Psi_0|^2$ corresponding to an initial set of parameters [40]. Therefore we minimize the estimate of s^2 given by

$$s_M^2 = \frac{\sum_{i=1}^M [E_L(\mathbf{R}_i) - E_g]^2 |\Psi(\mathbf{R}_i)/\Psi_0(\mathbf{R}_i)|^2}{\sum_{i=1}^M |\Psi(\mathbf{R}_i)/\Psi_0(\mathbf{R}_i)|^2} . \quad (31)$$

The major consideration for the stability and accuracy of the optimization is that s_M^2 accurately approximate s^2 . For this reason the ratio $|\Psi/\Psi_0|^2$ is included, reflecting the fact that Ψ changes as parameters are varied, although this requires computing parameter derivatives of Ψ . To enhance numerical precision, we adjust the normalization of Ψ so that $\sum_i |\Psi/\Psi_0|^2 = M$. This is useful for clusters with more than five atoms where changes in wave-function parameters have a large effect on the normalization of Ψ , because of its product form, and could make $|\Psi/\Psi_0|^2$ uniformly exceedingly large or small. The remaining determinant of the accuracy of s_M^2 is the number of points in the fixed sample. While a large number of points is desired for high accuracy, M is limited by considerations of computational cost and memory requirements. M is chosen so that the statistical error in the average of E_L over the points is significantly less than the desired improvement in the energy. We have employed 1000–2000 points for the smaller clusters, $\text{He}_{3-5,7}$, and 5000 points for He_{14} and He_{20} .

The final step in obtaining reliable optimizations involves updating the fixed sample. As the wave function changes, the points sampled from $|\Psi_0|^2$ become a poorer choice for computing expectation values with respect to $|\Psi|^2$. This is most noticeable when Ψ_0 is of poor quality and Ψ changes significantly during optimization. One manifestation of this degradation of the fixed sample is divergence of the energy to unrealistically low values. Therefore we have found it useful to update the sample by using a Metropolis walk to generate a new set of points sampled from the current wave function (which then plays the role of Ψ_0 .) Updating is implemented after the energy has converged or when it begins to diverge.

While the conjugate-gradient technique has been successful for the 3–20-atom clusters, it appears to be much less practical for larger clusters. (For He_{112} we started with the optimized He_{20} parameters and only reoptimized the long-range parameters by hand.) As the number of atoms in the cluster increases, the dimensionality of configuration space which must be represented by the fixed sample of points increases. Therefore larger samples are generally required for the larger clusters.

V. RESULTS AND DISCUSSION

A. Metropolis walks

As discussed in Sec. II, wave-function expectation values may be computed by the Metropolis approach. We first consider H_2He . Since the wave function depends only on the distance of He from the midpoint of H_2 , r , the walk takes place in only three dimensions, \mathbf{r} .

We start with the unguided walk employing several values of Δ in the range 11–40 Å and $M \approx 5 \times 10^7$. We find that sampling $|\Psi|^2$ for such a diffuse system is not

trivial. The energy is reproduced reasonably well, the computed value is generally within one or two standard deviations of the analytic, and the average error is 0.1%. However, we find sizable errors in $\langle r \rangle$ and $r_{\text{rms}} = (\langle r^2 \rangle)^{1/2}$. The smallest value of Δ produces errors of 6% and 7% in $\langle r \rangle$ and r_{rms} , respectively. Apparently, poor efficiency in sampling $|\Psi|^2$ occurs in this case. Upon increasing Δ to 27 Å, giving an acceptance ratio close to the often assumed optimum of 0.5, errors in $\langle r \rangle$ and r_{rms} are reduced to 1% and 2%, respectively. Interestingly, we find that only at a large value of Δ , 40 Å, and a relatively small acceptance ratio of 0.35, is accuracy in $\langle r \rangle$ and r_{rms} comparable to that of the energy, i.e., $\approx 0.1\%$.

The average displacement of the moves, $\langle \Delta \mathbf{r} \rangle$, sheds light on this behavior. We find that $\langle \Delta \mathbf{r} \rangle$ monotonically increases from 2.4 Å at $\Delta = 11$ Å to 4.7 Å at $\Delta = 40$ Å, correlating with the monotonic increase in the quality of $\langle r \rangle$ and r_{rms} . The fact that the local energy is relatively constant at large r , so that the computed energies are only weakly dependent on the accuracy of the sampling in this domain, readily explains the difference in behavior of the energy versus the coordinate expectation values.

As a precursor to DMC, we also performed guided-walk calculations with $\Delta = D\tau$ and $\mathbf{F} = \nabla \ln |\Psi|^2$. Note that T in Eq. (3) is now equivalent to G_a , Eq. (10), if the branching is omitted. We now encountered difficulty in sampling this distribution because of the sharp cutoff at small r . In computing at $\tau = 5 \times 10^4$, 10×10^4 , and 20×10^4 hartree $^{-1}$, we found large errors in the energy, 1% for the first two time steps and 5% for the last, despite the large number of points sampled, $M = (3-6) \times 10^7$. The behavior of the computed values of $\langle r \rangle$ and r_{rms} is, however, much different. Good accuracy and precision are obtained for these quantities at $\tau = 10 \times 10^4$ and 20×10^4 hartree $^{-1}$.

The reason for the poor estimates of the energy is that walkers are either trapped at smaller separations or else they do not sample these domains. This trapping is caused by the guiding force \mathbf{F} being excessively large at small r , where it is proportional to r^{-6} , giving acceptance probabilities practically equal to zero. This in turn yields a poor representation of the density at small r which does affect the computed energy because of the large magnitude of E_L there. This is much less significant for r and r^2 which are relatively small near the origin. Since the effect of \mathbf{F} on the acceptance probability is removed exponentially fast as $\tau \rightarrow 0$, the small- r domain is more accurately sampled as τ is reduced. However, efficiency is reduced at small τ because the small average step size gives a larger degree of correlation between moves.

We now consider the pure helium clusters. These systems possess a highly repulsive potential as does H_2He but are more tightly bound. (For example, the binding energy of He_3 is five times greater than that of H_2He .) This causes the computation of expectation values by an unguided walk to be less difficult than for H_2He , presumably because sampling a slowly decaying distribution at large r is no longer required. Despite sampling fewer points in calculations on $\text{He}_{3-5,7}$ [$M = (2-6) \times 10^8$ versus 5×10^7 for H_2He], for each cluster we observe excellent

agreement between computed expectation values over a range of Δ . For example, with $2.6 < \Delta < 13.2 \text{ \AA}$ for He_4 , the maximum difference in $\langle r \rangle$ (the average particle separation) is only 0.15% and that in the energy is only 0.07%.

While computed averages do not vary significantly as Δ is changed, statistical error in coordinate expectation values, $\langle r \rangle$ and R_{rms} [$R_{\text{rms}} = (\langle R^2 \rangle / N)^{1/2}$, where $R^2 = \sum_{i=1}^N (r_i - R_{\text{c.m.}})^2$], decreases as Δ (and $\langle \Delta R \rangle$) increases. In going from the smallest to the largest values of Δ , statistical error in R_{rms} and $\langle r \rangle$ is continuously reduced down to a factor of 2 or more, resulting in a four-fold or greater increase in computational efficiency for these quantities. For the energy, small values of Δ result in low efficiency. However, once Δ , and thereby $\langle \Delta R \rangle$, is of reasonable size, statistical error in the energy is no longer decreased as Δ is increased.

Overall, we find the average displacement $\langle \Delta R \rangle$ to be a useful measurement of the sampling efficiency in that larger values tend to give smaller statistical errors, most noticeably for R_{rms} and $\langle r \rangle$. We point out here that the sampling required to obtain $\langle \Delta R \rangle$ to high precision is quite small. Therefore finding the value of Δ which yields the greatest average displacement may be accomplished with very little computation. Finally, as was the case with H_2He , the acceptance ratios corresponding to the largest $\langle \Delta R \rangle$ were less than 0.5, i.e., 0.38 for He_4 and 0.40 for He_5 .

We now turn to the guided walk, which encounters difficulty when sampling at small r for H_2He and does not, therefore, appear useful for helium clusters. However, since the DMC walk we employ consists of the guided walk described above with branching, evaluating the practicality of this guided walk is important in ascertaining the feasibility of our DMC approach for obtaining exact results.

As discussed in Sec. IV, acceptance probabilities in the guided walk globally increase as the time step is reduced. If a time step can be found which is small enough to remove trapping at small r , so that convergence in sampling $|\Psi|^2$ can be obtained, without excessively degrading sampling efficiency, DMC may be practical for helium (and other) quantum clusters. Therefore we now determine values of τ which yield high accuracy in the guided walk for He_{3-5} .

Table II presents guided-walk energies and statistical errors (per point sampled) for He_{3-5} at several values of τ . The effect of trapping is immediately evident from the data in Table II. At the larger time steps the energies are of poor quality. In these walks we have observed that atoms which are too close together do not move during the entire course of a run. (Trapping is found by recording the number of accepted moves for each particle.) As the time step is reduced, particles are no longer trapped throughout the run. The result is a noticeable (and for He_5 a dramatic) improvement in the energy. Finally, we see that at sufficiently small time steps, guided-walk energies are in excellent agreement with those computed by the unguided approach.

The small- r behavior of the sampling, and its dependence on τ , is illustrated in Fig. 1. This figure compares

TABLE II. Guided-walk results for He_{3-5} . Time steps are given in hartree $^{-1}$, lengths are in \AA , and energies are in K.

$10^{-4}\tau$	$\langle \Delta R \rangle$	E/N	$\sigma(E/N)$
He_3			
25.00	2.14	-0.0369(33)	7.4
12.50	1.60	-0.0367(27)	6.0
5.00	1.09	-0.0381(14)	3.1
2.50	0.80	-0.0397(16)	5.1
1.25	0.58	-0.0418(7)	4.4
0.75	0.45	-0.04141(12)	1.1
Unguided	2.78	-0.04147(7)	0.14
He_4			
25.00	1.86	-0.1269(26)	7.4
15.00	1.55	-0.1288(6)	2.1
10.00	1.34	-0.1281(3)	1.1
5.00	1.04	-0.1329(23)	9.2
2.50	0.78	-0.1363(19)	10.7
1.25	0.57	-0.1361(7)	4.4
Unguided	2.21	-0.1356(1)	0.2
He_5			
10.00	1.17	-0.34(10)	200
5.00	0.96	-0.34(10)	200
2.00	0.69	-0.2487(12)	3.4
1.00	0.51	-0.25017(63)	2.2
0.50	0.37	-0.25048(51)	2.5
Unguided	1.65	-0.25023(13)	0.3

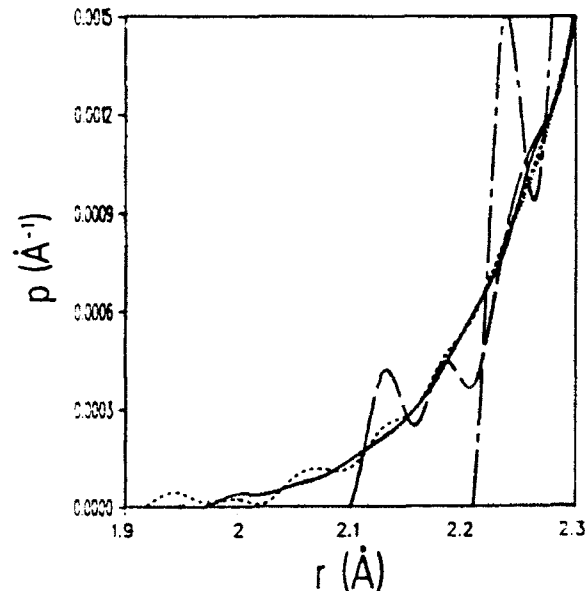


FIG. 1. Convergence of $p(r)$ at small r in the guided walk for He_3 . The solid line (—) is the unguided walk, the chain-dashed line (---) is the guided walk at $\tau = 50,000 \text{ hartree}^{-1}$, the long-dashed line (—) is at $\tau = 25,000 \text{ hartree}^{-1}$, the short-dashed line (---) is at $\tau = 12,500 \text{ hartree}^{-1}$, and the dotted line (· · ·) is at $\tau = 7,500 \text{ hartree}^{-1}$. Note the improving agreement between unguided and guided as the time step for the latter is reduced. The guided-walk energies follow the same trend, see Table II.

the probability density functions $p(r)$ at small particle separations (r) corresponding to several values of τ , with that of the unguided walk for He_3 . Fluctuations in p indicate trapping in certain regions and lack of penetration into others. These fluctuations decrease as τ is reduced, resulting in convergence to the unguided probability density function and agreement in the computed energies.

It is important to point out that the error in the energy at the larger time steps is not systematic. The trapping of points, or conversely the inability to sample certain domains at small particle separation (for a practical amount of sampling), will result in energies either too high or too low, depending on the sign of the local energy at small r and whether p is too high or too low. For the same reasons, statistical error may be artificially high or low when obtaining an accurate representation of $p(r)$ at small r is problematic.

For purposes of comparing efficiency with the unguided walk, the statistical error in the energy per point sampled, σ , is presented in the last column of Table II. For M points, σ is equal to the statistical error in the average times \sqrt{M} . This statistic depends on the sampling inefficiency of the algorithm, i.e., the degree to which successively sampled points are correlated, as well as the nonconstancy of E_L , which is determined by the wave function. Since Ψ is the same for the computations on a given cluster, algorithm efficiency may be directly compared. Table II shows that while agreement with unguided energies is obtained by the guided walk at sufficiently small τ , the unguided walk is consistently more efficient, with σ an order of magnitude smaller, yielding a decrease in computational efficiency of two orders of magnitude. Correspondingly, for the guided walk at the smallest time step, the average step size ($\langle \Delta R \rangle$) is four to five times smaller than that for the unguided walk. Nevertheless the guided walk still gives good precision for reasonable computational effort. If this is also the case with the DMC approach, the increase in accuracy will be well worth the computational effort.

The guided-walk approach we have employed is inefficient because of the rapid increase in the guiding force as atoms coalesce. This suggests that a guided-walk approach with a better behaved force will not encounter the difficulties found here. We have investigated two such choices in a few selected applications. The first, "weighted unit force," approach simply employs $c\hat{F}_i$ in place of $F_i = \nabla_i \ln|\Psi|^2$ when moving particle i . Thus the direction of the original F is preserved while its magnitude c is held constant. In the second, a "damped force" approach, $\chi_i F_i$ replaces F_i , where

$$\chi_i = \exp \left[\sum_{j, j \neq i} t_2(r_{ij}) \right], \quad (32)$$

and α_0 in t_2 becomes an adjustable parameter. Once again, the direction of the force is left unchanged but now its magnitude is most greatly affected only in the trapping regions, i.e., $|\chi_i F_i| \rightarrow 0$ when $\Psi \rightarrow 0$.

For the H_3He test case the parameters governing the force, c and α_0 , are varied together with τ to obtain maximum $\langle \Delta R \rangle$, which is roughly the same for the two guided walks. Trapping is not observed in either case and

values of $\langle \Delta R \rangle$ are obtained which are a factor of 2 greater than the maximum obtainable in the unguided walk. However, the statistical error in the energy shows little variation among the unguided, weighted, and damped approaches. On the other hand, guided-walk statistical errors in both $\langle r \rangle$ and r_{rms} are about 25% lower than those of the unguided walk.

For the second test case, He_{112} , only the damped force approach was compared against the unguided walk. While exhibiting no trapping, the damped force walk yielded no increase in efficiency over the unguided walk. Therefore we conclude that the simple unguided walk is competitive with the guided-walk approaches studied here.

B. DMC Computations on helium clusters

For the DMC walks, inaccurate sampling at small r can have an effect significantly greater than that observed for the guided walk. If points are temporarily trapped in a region where the local energy is very low, as we have seen can easily occur at small r , the branching factor will be very large, resulting in a quickly increasing number of walkers at small r . Although the particles trapped at a small separation may move to larger r after a short period of time, the continuous generation of new walkers at this point will yield a high degree of oversampling and thereby a highly biased (too low) energy. Therefore, at a given time step, trapping may not be problematic for the guided walk but nevertheless gives instability in the DMC approach. So we expect that smaller time steps will be required to obtain convergence in the DMC walk than in the guided walk. This is investigated below.

Given the instabilities possible in DMC, we take two steps to monitor the behavior of the walk. First, we allow the ensemble to only reach twice (or four times for the larger clusters) its original size. If the maximum ensemble size is attained, this event is recorded and all weights are carried so that the copying of walkers is no longer employed. To some extent this step controls instabilities arising from trapping in that the continuous replication of trapped walkers is not permitted. Additionally, if the weight of any walker exceeds a given value (10), the weight is recorded in the output file.

Results for the energy and its growth estimate E_G are presented in Table III and plotted in Figs. 2(a)–2(c) for He_{3-5} . Block length, on the order of 10^3 – 10^6 hartree $^{-1}$, was varied by factors of 2–4 resulting in no significant change in the computed energies. Also, maximum ensemble sizes (200) and excessive weights (10), while found at the larger time steps, were not observed at the smaller (last two or three) values of τ . Given this, and the statistical agreement of the energies at the smaller time steps, the DMC energies we have computed are deemed to be well converged. However, we do see that much smaller values of τ are indeed required than was the case for the guided walk; approximate comparisons are 1000 versus 12 500 hartree $^{-1}$ for He_3 , 1500 versus 25 000 hartree $^{-1}$ for He_4 , and 1500 versus 10 000 hartree $^{-1}$ for He_5 (compare Tables II and III).

Umrigar, Runge, and Nightingale have recently de-

TABLE III. DMC energy vs time step for $\text{He}_{1,5}$. The average of the local energy is E and the growth estimate is E_G . Time steps are given in hartree $^{-1}$, lengths are in Å, and energies are in K. AR denotes the acceptance ratio.

$10^{-3}\tau$	AR	$\langle \Delta R \rangle$	E/N	E_G/N
He_3				
4.0	0.9963	0.62	-0.0486(14)	-0.0447(7)
3.0	0.9975	0.54	-0.0462(7)	-0.04428(35)
2.0	0.9986	0.44	-0.04433(16)	-0.04406(17)
1.0	0.9995	0.31	-0.04409(18)	-0.04398(17)
0.5	0.9998	0.22	-0.04428(20)	-0.04393(23)
He_4				
5.0	0.9908	0.69	-0.1750(90)	-0.1455(7)
2.5	0.9965	0.49	-0.1514(38)	-0.1454(6)
2.0	0.9975	0.44	-0.1481(16)	-0.1457(7)
1.5	0.9983	0.38	-0.1445(3)	-0.1448(4)
1.0	0.9991	0.31	-0.1445(3)	-0.1444(3)
He_5				
2.0	0.9963	0.45	-0.282(13)	-0.2682(8)
1.5	0.9975	0.38	-0.2683(5)	-0.2675(4)
1.0	0.9986	0.31	-0.2673(11)	-0.2674(10)

scribed a DMC approach which controls the magnitude of F near its singularities and yields a better approximation to the Green's function in this domain [41]. It will be of interest to see if this method will reduce time-step bias, and thereby increase efficiency by allowing greater values of τ , in DMC computations on helium clusters.

Neglecting the different time-step scales, the behavior of the DMC energies is very similar to those of the guided walk. In essence, both walks are affected by trapping, which is magnified by the branching in the DMC walk. As was also the case for the guided walk, the coordinate expectation values, $\langle r \rangle$ and R_{rms} , were not visibly affected by τ . This is not surprising as these quantities are only weakly influenced by sampling accuracy at small particle separations. This lack of time-step bias is also seen for the particle separation density functions $p(r)$ (except of course at small r), as well as for the density profiles.

Computational cost in obtaining converged DMC energies was large but not excessive. While He_3 presented an especially difficult case requiring five Cray X-MP14 CPU hours for all (not each) of the time steps, He_4 and He_5 took only one and two hours, respectively. As for H_2He at the VMC level of theory, the smallest and most diffuse cluster gave the greatest difficulty in obtaining the accuracy and precision desired.

Having successfully obtained converged energies for the smaller clusters, it was of interest to see if this could also be achieved for the larger clusters. We found for He_N , $N=7, 14, 20, and 112 , DMC energies converged at about $\tau=500-1500$ hartree $^{-1}$. Even at the largest time step of 2000 hartree $^{-1}$, the energies were very close to those computed at the smallest values of τ . Overall, the dependence of E/N and E_G/N versus the time step mimics that of the smaller clusters. At "larger" τ (≈ 2000 hartree $^{-1}$), bias is noticeable and large weights and fluctuations in ensemble size occur. At "smaller" τ ($\approx 1000$$

hartree $^{-1}$), stability in the DMC energies, weights, and ensemble sizes is obtained. Therefore, while the required time step for unbiased energies is greatly reduced for DMC versus the guided walk, this is not the case for larger clusters versus smaller clusters. Unbiased energies are obtained at $\tau=1000-1500$ hartree $^{-1}$ for 3-5 atoms and $\tau=500-1500$ hartree $^{-1}$ for 7, 14, 20, and 112 atoms. (Here, absence of bias, i.e., it being masked by statistical error, is relative rather than absolute. For example, a bias of 0.005 K is very large for He_3 , 11% of E/N , but on the order of the statistical error for H_{112} , 0.1% of E/N .) This is explained by the fact that convergence in DMC is most affected by trapping combined with large fluctuations in the local energy at small r —effects which are governed mostly by the wave-function form rather than by cluster size. Total computational cost was roughly 2, 4, 5, and 17 Cray X-MP14 CPU hours for $N=7, 14, 20$, and 112, respectively.

The DMC results are summarized and compared to GFMC [10,11] and other recent DMC results [18] (He_{20} and He_{112}) in Table IV. The results we compare against were obtained with the HFDHE2 potential [32] which predates the most recent, HFD-B(HE), potential [31] used here. The two potentials possess practically identical functional forms but with different sets of parameters. Perhaps most significant is the 1.3% increase in well depth. For the unit radius, $r_0 \equiv \sqrt{5/3} R_{\text{rms}}/\sqrt{N}$, we employ a "second-order" approximation of exact expectation values [7] defined as

$$\langle A \rangle_s \equiv 2\langle \Psi | A | \phi_0 \rangle / \langle \Psi | \phi_0 \rangle - \langle \Psi | A | \Psi \rangle, \quad (33)$$

with $A = R^2$. Writing $\Psi = \phi_0 + \delta$ shows that $\langle A \rangle_s$ differs from the exact value, $\langle \phi_0 | A | \phi_0 \rangle$, by integrals involving δ^2 . (This approximation is useful when A does not commute with the Hamiltonian. Methods for computing $\langle \phi_0 | A | \phi_0 \rangle$ have been described elsewhere [42,43].)

The DMC energies we compute with the HFD-B(HE) potential are significantly below the GFMC energies resulting from the previous, HFDHE2, potential. The relative discrepancies tend to decrease with increasing cluster size. For He_3 our energy is 13% lower than the GFMC value while for He_{14} and He_{20} the differences are only 3.3% and 3.7%, respectively. However, as seen in Table IV, for He_3 and He_{20} our DMC energies are in excellent agreement with GFMC when the same potential (HFDHE2) is employed. In contrast, our HFDHE2 energy does not agree with GFMC for He_{112} . The new potential lowers our He_{112} DMC energy by 3.2%. Such sensitivity to small changes in the potential has been observed previously. Kalos *et al.*, employing the HFDHE2 poten-

tial in their study of liquid ^4He , obtained a 6% decrease in the energy for a 1.9% increase in the well depth [44].

Upon considering He_{112} and comparing with the DMC energies computed by Chin and Krotscheck [18] (CK), employing a DMC algorithm different than our own [45], discrepancies not attributable to the potential arise. For He_{20} , we see in Table IV that CK's energy is 2% below both our DMC and the GFMC values, when all three calculations employ the same (HFDHE2) potential. For He_{112} , further disagreement occurs with the same potential as our and CK's energy lie roughly 2% and 3%, respectively, below GFMC. This is not readily explained by statistical error which, for both GFMC and DMC, is an order of magnitude smaller than these differences. It

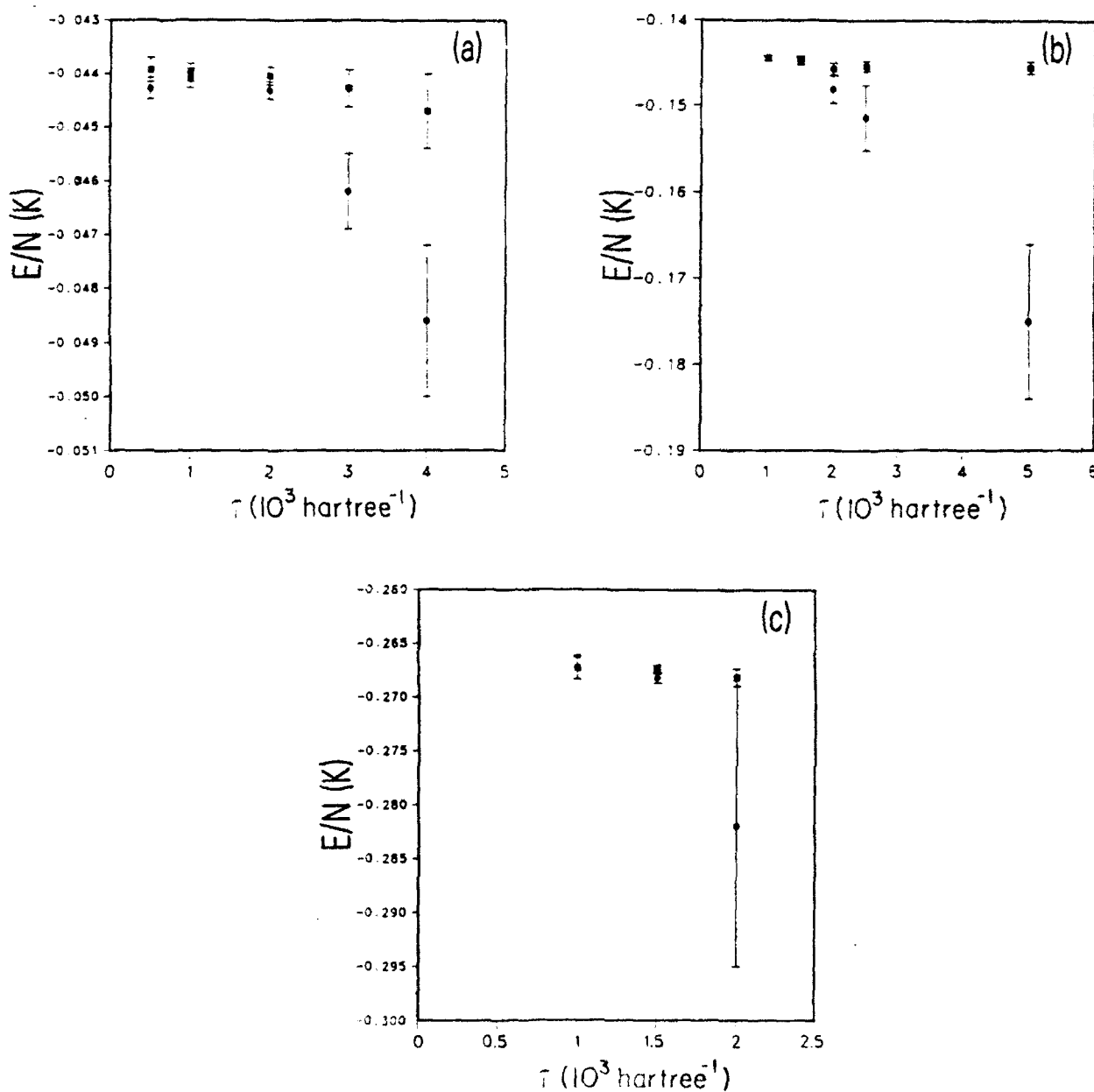


FIG. 2. Local (circles) and growth (squares) energy estimates of the exact energy vs τ for (a) He_3 , (b) He_4 , and (c) He_{20} .

tion has equilibrated. This was done for He_3 , reducing the discrepancy between the two energy estimates from 0.9% to 0.5%, thereby giving near statistical agreement.

For the unit radii r_0 , we first compare our DMC and the GFMC values for He_3 and He_{20} computed using the same potential (Table IV). While agreement is observed for He_{20} , a large difference of 8% is seen for He_3 . This difference is well beyond our statistical error of 1%. (Except for He_3 , statistical error in DMC values of r_0 is well under 1%, i.e., 0.01–0.02 Å.) Furthermore, this disagreement with GFMC does not appear to be caused by error in our second-order estimate of r_0 . The error in the second-order estimate of r_0 , $\approx \langle \delta |R^2| \delta \rangle$, should be less than the difference between the VMC and DMC values, $\approx \langle \delta |R^2| \Psi \rangle$, which is only 2%. For the largest cluster, $N = 112$, disagreement resurfaces when comparing our value of r_0 against GFMC obtained with the

same potential. The difference between our VMC and DMC values is only 0.6%, implying an error of much less than 0.6% in the second-order estimate. Statistical error in the second-order values, 0.003 Å or less, cannot be the cause of the 2% discrepancy between second-order DMC and GFMC.

The unit radii computed by CK differ slightly from our own, 1.5% below for He_{20} and 0.8% above for He_{112} . These differences are most likely caused by the differences in the DMC solutions obtained, as reflected by the energies, rather than by the second-order approximation. This is supported by the fact that CK also obtain very good agreement between their VMC and second-order unit radii.

Finally, in comparing results using the HFD-B(HE) potential for He_{112} , we note that the difference between VMC and DMC is only 0.6%. Therefore, in this case, we

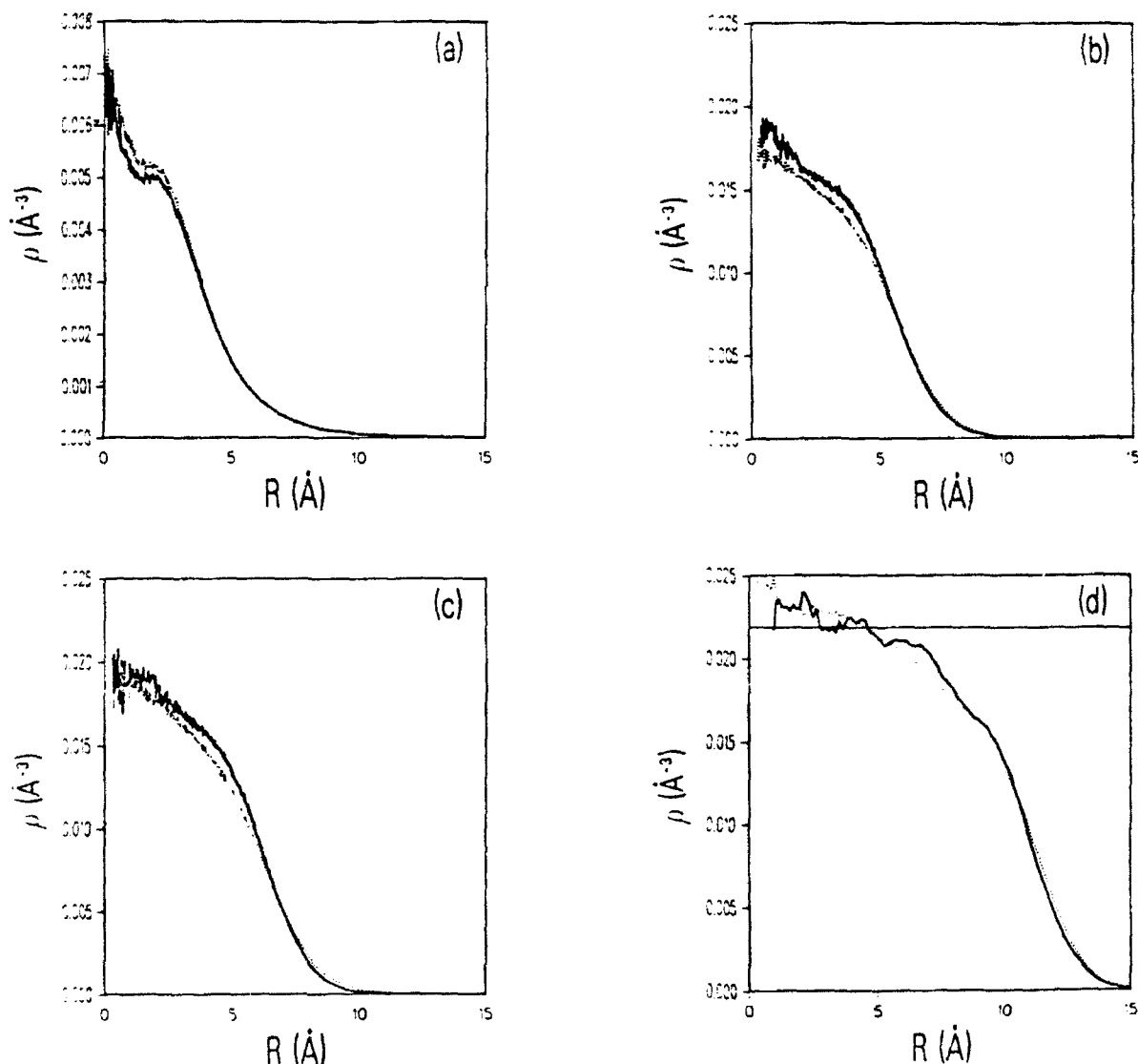


FIG. 3. VMC and second-order density profiles for (a) He_3 , $\tau = 500$ hartree⁻¹, (b) He_{14} , $\tau = 500$ hartree⁻¹, (c) He_{20} , $\tau = 750$ hartree⁻¹, and (d) He_{112} , $\tau = 1000$ hartree⁻¹. The dotted line is the VMC and the solid line is the second-order approximation to the exact [Eq. (33)]. The straight line in (d) represents the experimental liquid-helium density of 0.02185 Å^{-3} .

also expect our computed value of r_0 to be accurate to the number of figures shown. The change in r_0 on comparing the old- versus the new-potential values (2.396 versus 2.390 Å) is only 0.3%, significantly less than the 1% difference we find for He_{20} . In all cases where comparison is made, r_0 is reduced when employing the potential with the deeper well, as expected. This effect decreases by an order of magnitude, 3.8% to 0.3%, in passing from three to 112 atoms and contrasts with the change in the energy, 13.2% to 3.2%.

Of greater interest is the reliability of our reported estimates of r_0 obtained with the most up-to-date potential. We have found that the differences between VMC and DMC reach a maximum of only 3% (He_4 and He_3).

Therefore we expect an accuracy of at least 3% in our estimates of r_0 . However, the accuracy is probably much better; for He_3 0.5% agreement is obtained from wave functions with noticeably different VMC values of r_0 , 5.50 and 5.74 Å, i.e., above and below the estimated exact value.

Figures 3(a)–3(c) present VMC and second-order ($\tau=500$ –1000 hartree⁻¹) [see Eq. (33)] density profiles for He_3 , He_{14} , and He_{20} . The bin sizes are very small, 0.026 Å for He_3 and 0.019 Å for He_{14} and He_{20} . This allows for very fine detail in ρ , and although there is enhanced statistical error near the origin, it remains below 10% down to about 0.2–1 Å. We see for these clusters, as well as for the other clusters not shown, that

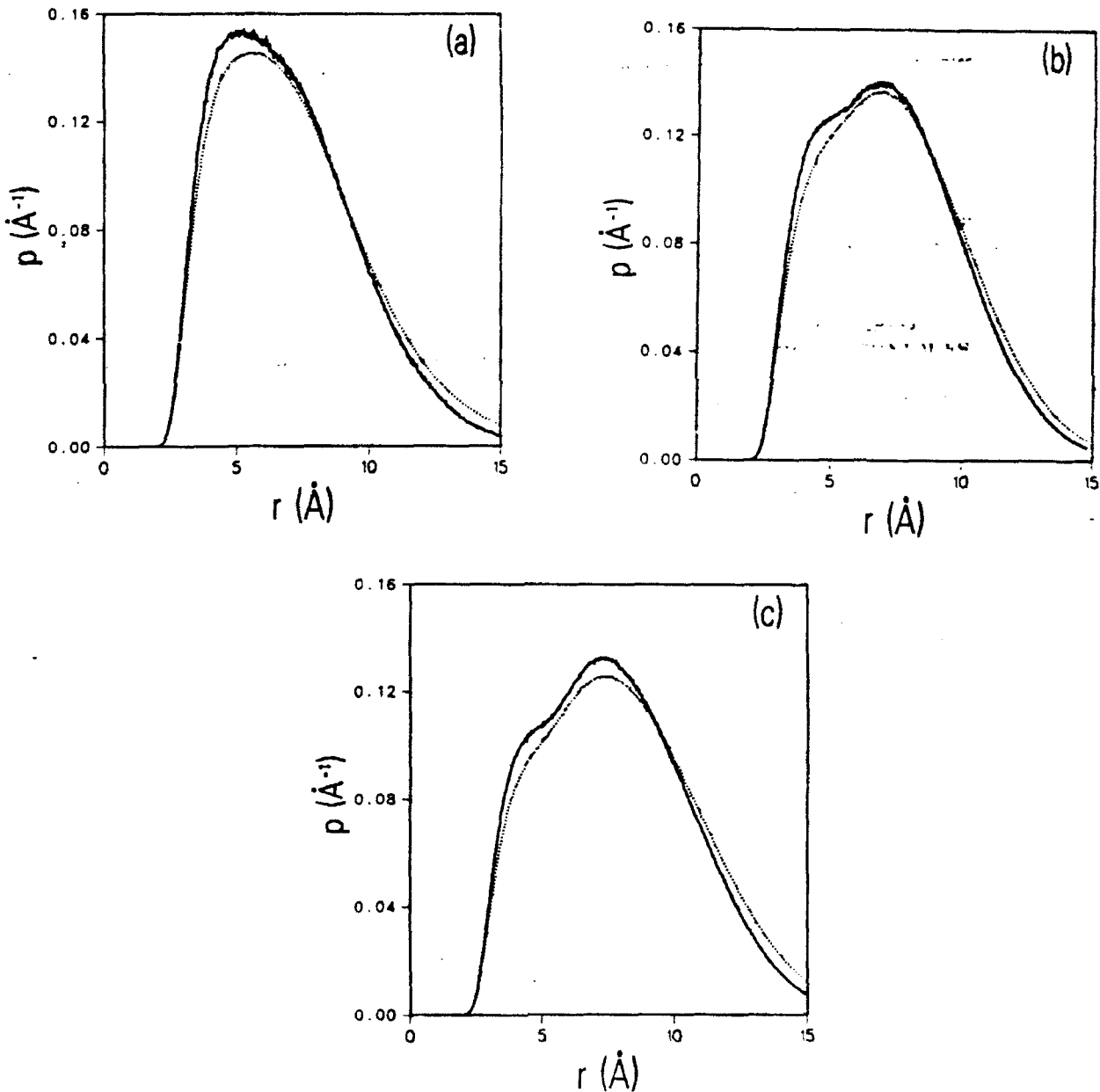


FIG. 4. VMC and second-order probability density functions of particle separation for (a) He_3 , $\tau=500$ hartree⁻¹, (b) He_{14} , $\tau=500$ hartree⁻¹, and (c) He_{20} , $\tau=750$ hartree⁻¹. The dotted line is the VMC and the solid line is the second-order approximation to the exact.

es-
-ich
ave
 r_0 ,
act
for
les
ill,
al-
is
ns
se
at

the qualitative behavior is unchanged between the VMC and second-order profiles. The sharp increase in ρ near the cluster center for He_3 , which we first observed at the VMC level of accuracy and which arises from a significant contribution of near-collinear configurations to the density [28], remains in DMC. For 14- and 20-atom clusters, very little structure is evident. The He_{14} density rises slightly near the origin while that of He_{20} reaches a constant value at about 2.5 \AA and then fluctuates about 0.019 \AA^{-3} . This is in good agreement with GFMC [10] and the oscillations seen by CK are not observed here.

VMC and second-order ($\tau = 500 \text{ hartree}^{-1}$) density profiles for He_{112} are computed with a bin size of 0.13 \AA and are presented in Fig. 3(d). The experimental liquid-helium density of 0.02185 \AA^{-3} is shown for comparison as a solid line. Statistical error is 10% for the points nearest the origin, then decreases rapidly at greater distances, and finally begins to rise near the cluster edge, reaching about 10% at 11 \AA . Unlike any of the smaller clusters, structure in the density profile now appears to be present. However, further analysis indicates that the fluctuations at $R < 5 \text{ \AA}$ are statistical. Only in a very small region, $2.10-2.35 \text{ \AA}$, is statistical error (4.5%) significantly below the deviation from the liquid density (6%-10%). Thus, out to 4.8 \AA , the density is very nearly constant to within reasonable statistical error (under 5% for $R > 1.5 \text{ \AA}$). However, a shoulder is present at 6.2 \AA where statistical error is very small, 1.5%. Further out, another shoulder at 9.6 \AA is barely discernible. This is in good agreement with CK (bin size is 0.24 \AA), who also observe shoulders in these regions. We have also computed a second-order density profile for He_{112} employing the HFDHE2 potential. The results are very similar to those we obtained above.

In summary, our second-order densities for $N = 14, 20$, and 112 rise up to their central values at some distance from the origin. The value of this central density and the distance to which it extends increases with cluster size. The He_{14} central density is clearly below that of liquid helium and ρ begins to drop off at about 1 \AA . That of He_{112} is in good agreement with the liquid-He density and extends out to about 4.5 \AA while the He_{20} case is intermediate between He_{14} and He_{112} . These conclusions differ from those of CK, who obtain oscillations in their density profiles as the origin is approached for both He_{20} and He_{112} . We see no such oscillations for He_{20} while those of He_{112} are mostly removed upon considering the small (2%-5%) statistical error. However, we do see shoulders in the He_{112} density at larger R .

For all clusters, the quantitative differences between the VMC and second-order density profiles are not large. The small changes we observe in passing from VMC to second order lead us to believe our estimate of exact density profiles by second-order profiles is well justified (see discussion concerning the unit radii). Comparison against density profiles computed by VMC [26] or GFMC [10] shows little variation in the central density, despite the different potentials and wave functions employed. A major difference does arise for He_3 which has

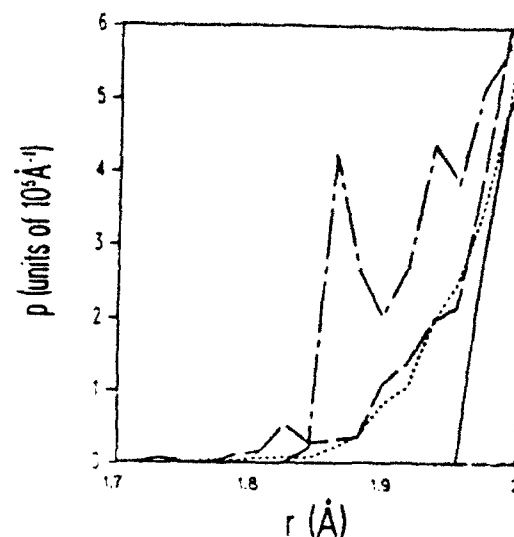


FIG. 5. VMC (—) and DMC plots of $p(r)$ at short range for He_{14} at $\tau = 2000$ (---), 1000 (— · —), and 500 (· · · · ·) hartree^{-1} .

a sharp increase in ρ at about 2 \AA [28] which is not evident in GFMC [10].

In order to gain further insight into cluster structure and its changes as accuracy is improved from VMC to the second-order approximation, we compute particle separation probability density functions $p(r)$. Figures 4(a)-4(c) present VMC and second-order plots of $p(r)$ for He_3 , He_{14} , and He_{20} . For He_{3-5} , qualitative distinctions are not discernible between the VMC and second-order density functions, just as for He_3 . For those clusters which show structure in p with VMC, He_{14} and He_{20} , qualitative differences between VMC and second-order densities are now apparent. We see that the implied shoulder in p found by VMC becomes much more pronounced as we progress to the second-order level of accuracy. It would be interesting to see if this onset of "shell" structure is progressive or abrupt as cluster size is increased from 7 to 14 atoms. We point out once more that both ρ and p are essentially independent of the time step employed (for the range of τ we have considered). The exception of course is for p at small r . An example of this is given in Fig. 5 which presents the VMC and several second-order estimates in the region $p(r)/p_{\max} < 5 \times 10^{-4}$ for He_{14} . Note that by $\tau = 1000 \text{ hartree}^{-1}$ convergence is quite good, as is the case for the energy. (See Table IV and associated discussion.)

C. New two-body form and T_2

We have employed our new two-body form, t_2' [see Eq. (24)], in unguided-walk computations on He_N , $N = 3, 7$, and 20 . For each cluster the same value of Δ is employed for t_2 and t_2' . We find that t_2 yields the best energy for He_3 , 5% below that of t_2' . However, for the larger clusters, small but significant (i.e., well beyond statistical error) reductions are obtained with t_2' , i.e., 2% for He_7 and 1% for He_{20} . For He_3 , the most diffuse cluster, the re-

duced flexibility of t'_2 in describing long-range behavior is significant. In addition to yielding a poorer energy, t'_2 also gives an unrealistically low unit radius. For the more tightly bound clusters, for which short-range interactions are more important, an improvement with t'_2 is obtained. Also, t'_2 yields a 30% reduction in statistical error in the energy, even for He_3 , presumably by better describing the short-range behavior where the local energy possesses its greatest fluctuations. Consequently, we expect that further accuracy may be obtainable by increasing the long-range flexibility of t'_2 .

In addition to seeking better two-body wave functions, accuracy can also be increased by including three-body (and higher) effects, as discussed in Sec. IV A. We treat here the larger clusters, whose wave functions should possess the greatest need for three-body correlations. For He_{14} and He_{20} , the initial parameters in T_2 (t_2 here) are obtained from a conjugate-gradient optimization. For He_{112} initial parameters are those for He_{20} and are then varied by hand. As seen in Table I, optimization resulted from changing only the long-range parameters. Upon addition of T_3 , parameters are varied by hand in a set of short Monte Carlo runs. At this stage, only variation of the T_3 parameters and of the long-range parameters in T_2 was found to be fruitful. Despite the approximate level of optimization, a significant reduction in the energy is observed in all cases. The optimized T_3 term yielded about a 6% improvement in the energy for He_{14} and He_{20} . As expected, the He_{112} energy is reduced by a greater amount (9%) than for the smaller clusters. The final result is that the VMC energies of the $N = 14, 20$, and 112 clusters are quite good; 96.1% of the computed exact value is obtained for He_{14} and this decreases only by 1.5% upon going to He_{112} .

Wave-function quality is also improved in other respects. The data listed in the middle of Table V show that the relative statistical error in the energy decreases in every case. The increased computation when T_3 is in the wave function ranges from 82% for He_{14} to 88% for He_{112} . Allowing for this, the efficiency (the inverse product of the variance and the computation time) in computing the energy is increased by a factor of 2 for He_{14} and He_{112} . Interestingly, however, efficiency is decreased by 19% for He_{20} . This contrast with the He_{14} and He_{112} cases may arise from incomplete (hand) parameter optimization or from use of the energy, rather than variance, minimization criterion. It could also be magnified by the generally large uncertainties in computed statistical error.

TABLE V. Accuracies and precisions for two- and three-body wave functions.

N	Accuracy in E/N		$\sigma(E/N)/(E/N)$		Accuracy in r_0	
	T_2	$T_2 + T_3$	T_2	$T_2 + T_3$	T_2	$T_2 + T_3$
14	90.5	96.1	1.00	0.52	3.2	1.2
20	89.5	95.3	0.93	0.76	4.7	2.8
112	85.7	94.6	0.23	0.11	4.9	1.2

In the last two columns of Table V, percent differences between VMC and second-order unit radii r_0 are listed for the T_2 and $T_2 + T_3$ wave functions of He_{14} , He_{20} , and He_{112} . We expect these differences to be good estimates of the deviation from exact values, given our confidence in the accuracy of our second-order estimates of r_0 , see Sec. V B. In each case agreement with second-order estimates of r_0 is noticeably enhanced upon addition of the three-body correlation functions. The result is that very good agreement ($\approx 1\%$) with estimated exact unit radii is obtained at the VMC level of theory with the three-body wave functions. The exception is again He_{20} with a VMC value of r_0 differing by 3% from the second-order estimate.

VI. CONCLUSIONS

We have studied wave-function forms and Monte Carlo integration techniques for H_2He and He_N , $N = 3-20,112$. As a very diffuse system with a highly repulsive potential, H_2He presented special difficulties for the VMC computations. While the VMC approaches used here are without bias, errors in computed quantities can arise for a finite (yet large) amount of sampling if efficiency is sufficiently poor. Therefore only for very large attempted displacement sizes Δ is good accuracy obtained in the unguided walk. Furthermore, these values of Δ correspond to acceptance ratios of 0.35-0.40, well below the often assumed optimum of 0.5.

Despite the increased dimensionality in comparison to H_2He ($3N$ versus 3), the less diffuse helium clusters are much more amenable to Monte Carlo integration. For the unguided walk, consistency in computed expectation values is obtained over a wide range of Δ . However, we do find that statistical error in both $\langle r \rangle$ and r_{rms} is noticeably lower at large Δ . Once again, these values of Δ corresponded to the largest average displacement of an attempted move, $\langle \Delta R \rangle$, rather than to an acceptance ratio of 0.5.

Directly including importance sampling by using a walk guided by $\mathbf{F} = \nabla \ln |\Psi|^2$ yielded inaccurate H_2He energies. Although most of configuration space was well sampled, as indicated by accurate values of $\langle r \rangle$ and r_{rms} , large values of the force \mathbf{F} caused trapping at small r . The resulting inaccuracy in the density gave rise to significant errors in the computed energy because, although the wave function is small, the large magnitude of the local energy at small separations requires accurate sampling in this region. However, trapping is readily circumvented by employing a better behaved force. Two such approaches, which still direct moves toward a local maximum in $|\Psi|^2$, were applied to H_2He and He_{112} . Compared to an unguided walk, efficiency was increased slightly for H_2He but not for He_{112} .

As seen for H_2He , errors in the energy arise in a walk guided by $\mathbf{F} = \nabla \ln |\Psi|^2$ due to poor convergence at small r (which is practically infinitely long unless τ is very small). In light of the desire to compute exact energies by DMC, however, it was of interest to determine the domain of r at which high accuracy could be obtained by this guided walk. We find that, though initially quite

poor at large τ , accurate energies are obtained at smaller values. "Convergence" in the guided-walk energies is directly correlated, as expected, with improving accuracy in $p(r)$ at small r as the time step is reduced. This was also the case in the DMC calculations, demonstrating that accuracy in the (DMC or VMC) energy is critically dependent on the sampling at small r . In light of this discussion, we point out that a DMC approach similar to that employed here but which bounds the magnitude of \mathbf{F} near $\Psi=0$ has been described recently [41] and may be of use for the systems studied here.

Although small time steps are required, well-converged DMC energies have been obtained for He_N , $N=3-5, 7, 14, 20, 112$. The steps taken to ascertain convergence, variation of the time step and block size, comparison of the local and growth energy estimates, and convergence of p at small r , all support the reliability of the computed energies. As we have already found with VMC for He_3 and He_4 [28], energies well below those of GFMC [10,11] are obtained. For He_3 and He_{20} , these discrepancies are clearly caused by the use of different potentials. It is reasonable to conclude that this is also the case for all the 3-20 atom clusters studied here. The agreement we obtain with GFMC for an identical potential leads us to believe in the reliability of our DMC approach and the exactness of our computed energies with the most up-to-date potential. However, energies below GFMC (but with the same potential) have been obtained by CK using a modified DMC approach for He_N , $N=20, 40, 70$, and 112 [18], and by us for $N=112$. While the discrepancy between DMC and GFMC is smaller in our calculation than in CK's, our energy is still significantly lower than the GFMC result. Further disagreement occurs when comparing our DMC energies with those of CK. For both $N=20$ and 112, we compute slightly higher energies.

We see a sizable lowering of the energy below that obtained from the earlier, HFDHE2, potential when employing the most recent, HFD-B(HE), He-He interaction potential, 13% for three atoms and 3.2% for 112. This reflects primarily the lower well depth of the newer potential. Decreases in the unit radius are also observed,

3.8% for He_3 to 0.3% for He_{112} . Finally, as do CK, we see fluctuations in the He_{112} density profile which have not previously been observed at either the VMC or GFMC level of theory. However, our fluctuations at small R are beneath statistical error as differences from the liquid-helium density are generally less than one standard deviation in this region, $R < 5 \text{ \AA}$.

In an effort to improve accuracy at the two-body level, we have studied an entirely new form describing these effects. This form gives added emphasis at small r and contains a factor which mimics the potential in this domain. Optimized wave functions for He_3 and He_{20} gave slightly improved energies, despite the reduced flexibility at large r . For the more diffuse He_3 , the older form gave a lower energy. In addition, statistical error in the energy was reduced by about a third. It is expected that a better description of the long-range behavior will yield further improvements.

In order to investigate the accuracy obtainable by current VMC approaches, a three-body factor was added to the 14-, 20-, and 112-atom two-body wave functions. Substantial improvement in the energy is obtained, and for He_{14} and He_{112} an increased efficiency in computing this quantity also results, despite the greater complexity of the wave function. More sophisticated optimization algorithms for the parameters in T_3 may yield a further lowering of the VMC energy. It also remains to be seen whether T_2' , combined with T_3 , will yield better agreement with exact energies, and whether the use of such complex wave functions will be advantageous for DMC.

ACKNOWLEDGMENTS

This work was supported by the Office of Naval Research under Grant No. N00014-89-J-1755, and by the National Science Foundation (Grant No. CHE-8907423). Acknowledgment is also made to the Donors of the Petroleum Research Fund, administered by the American Chemical Society, for partial support of this research. K.B.W. would also like to thank the Alfred P. Sloan Foundation for financial support.

- [1] For an up-to-date review, see Proceedings of the Fifth International Meeting on Small Particles and Inorganic Clusters, Konstanz, Federal Republic of Germany, 1990 [Z. Phys. D 19 (1991); 20 (1991)].
- [2] N. Metropolis, A. W. Rosenbluth, M. N. Rosenbluth, A. H. Teller, and E. Teller, J. Chem. Phys. 21, 1087 (1953).
- [3] M. H. Kalos and P. A. Whitlock, *Monte Carlo Methods* (Wiley, New York, 1986), Vol. 1, Chap. 3.
- [4] G. E. P. Box and M. E. Mueller, Ann. Math. Stat. 29, 610 (1958).
- [5] M. H. Kalos, J. Comput. Phys. 1, 257 (1966).
- [6] M. H. Kalos, D. Levesque, and L. Verlet, Phys. Rev. A 9, 2178 (1974).
- [7] P. A. Whitlock, D. M. Ceperley, G. V. Chester, and M. H. Kalos, Phys. Rev. B 19, 5598 (1979).
- [8] D. M. Ceperley and B. J. Alder, J. Chem. Phys. 81, 5833 (1984).
- [9] K. E. Schmidt and J. W. Moskowitz, J. Stat. Phys. 43, 1027 (1986).
- [10] V. R. Pandharipande, J. G. Zabolitzky, S. C. Pieper, R. B. Wiringa, and W. Helmbrecht, Phys. Rev. Lett. 50, 1676 (1983).
- [11] R. Melzer and J. G. Zabolitzky, J. Phys. A 17, L565 (1984).
- [12] J. G. Zabolitzky, in *Progress in Particle and Nuclear Physics*, edited by A. Faessler (Oxford, New York, 1986), Vol. 16, p. 103.
- [13] J. B. Anderson, J. Chem. Phys. 63, 1499 (1975).
- [14] D. R. Garner and J. B. Anderson, J. Chem. Phys. 86, 4025 (1987); 86, 7327 (1987).
- [15] P. J. Reynolds, D. M. Ceperley, B. J. Alder, and W. A. Lester, Jr., J. Chem. Phys. 77, 5593 (1982).
- [16] R. N. Barnett, P. J. Reynolds, and W. A. Lester, Jr., J. Chem. Phys. 77, 4992 (1986).

- [17] B. L. Hammond, M. M. Soto, R. N. Barnett, and W. A. Lester, Jr., *J. Mol. Struct.* **234**, 525 (1991).
- [18] S. A. Chin and E. Krotscheck, *Phys. Rev. B* **45**, 852 (1992).
- [19] H. Sun and R. O. Watts, *J. Chem. Phys.* **92**, 603 (1990).
- [20] M. A. Suhm and R. O. Watts, *Phys. Rep.* **204**, 293 (1991).
- [21] S. M. Rothstein and J. Vrbik, *J. Chem. Phys.* **87**, 1902 (1987).
- [22] J. B. Anderson and D. R. Garmer, *J. Chem. Phys.* **87**, 1903 (1987).
- [23] P. J. Reynolds, R. K. Owen, and W. A. Lester, Jr., *J. Chem. Phys.* **87**, 1905 (1987).
- [24] R. N. Barnett, Ph.D. thesis, University of California, Berkeley, 1989 (unpublished).
- [25] D. M. Ceperley, *J. Comput. Phys.* **51**, 404 (1983).
- [26] V. R. Pandharipande, S. C. Pieper, and R. B. Wiringa, *Phys. Rev. B* **34**, 4571 (1986).
- [27] M. V. Rama Krishna and K. B. Whaley, *J. Chem. Phys.* **93**, 6738 (1990).
- [28] R. N. Barnett and K. B. Whaley, *J. Chem. Phys.* **96**, 2953 (1992).
- [29] W. C. Meyer, P. C. Hariharan, and W. Kutzelnigg, *J. Chem. Phys.* **73**, 1880 (1980).
- [30] G. Schätz (private communication).
- [31] R. A. Aziz, F. R. W. McCourt, and C. C. K. Wong, *Mol. Phys.* **61**, 1487 (1987).
- [32] R. A. Aziz, V. P. S. Nain, J. S. Carley, W. L. Taylor, and G. T. McConville, *J. Chem. Phys.* **70**, 4330 (1979).
- [33] C.-W. Woo, *Phys. Rev. Lett.* **28**, 1442 (1972).
- [34] C. C. Chang and C. E. Campbell, *Phys. Rev. B* **15**, 4238 (1977).
- [35] V. R. Pandharipande, *Phys. Rev. B* **17**, 218 (1978).
- [36] K. Schmidt, M. H. Kalos, M. A. Lee, and G. V. Chester, *Phys. Rev. Lett.* **45**, 573 (1980).
- [37] Q. N. Usmani, S. Fantoni, and V. R. Pandharipande, *Phys. Rev. B* **26**, 6123 (1982).
- [38] The particular representation of T , given in Eqs. (27) and (28) is due to a private communication with S. C. Pieper.
- [39] For an excellent description, see W. H. Press, B. P. Flannery, S. A. Teukolsky, and W. T. Vetterling, *Numerical Recipes* (Cambridge University Press, Cambridge, England, 1986), pp. 301–306.
- [40] C. J. Umrigar, K. G. Wilson, and J. W. Wilkins, *Phys. Rev. Lett.* **60**, 1719 (1988).
- [41] C. J. Umrigar, K. J. Runge, and M. P. Nightingale, in *Monte Carlo Methods in Theoretical Physics*, edited by S. Caracciolo and A. Fabrocini (ETS Editrice, Pisa, 1991), p. 161.
- [42] K. S. Liu, M. H. Kalos, and G. V. Chester, *Phys. Rev. A* **10**, 303 (1974).
- [43] R. N. Barnett, P. J. Reynolds, and W. A. Lester Jr., *J. Comput. Phys.* **96**, 258 (1991).
- [44] M. H. Kalos, M. A. Lee, P. A. Whitlock, and G. V. Chester, *Phys. Rev. B* **24**, 115 (1981).
- [45] S. A. Chin, *Phys. Rev. A* **42**, 6991 (1990).